



B/PS bulges and barlenses from a kinematic viewpoint. I

Daria Zakharova^{1,2}  , Iliya S. Tikhonenko³, Natalia Ya. Sotnikova⁴, and Anton A. Smirnov⁵

¹*Dipartimento di Fisica e Astronomia "Galileo Galilei", Università degli studi di Padova, Vicolo dell'Osservatorio, 3, I-35122, Padova, Italy*

²*INAF - Osservatorio astronomico di Padova, Vicolo dell'Osservatorio, 5, I-35122, Padova, Italy*

³*Max-Planck-Institut für extraterrestrische Physik, Gießenbachstraße, D-85748 Garching, Germany*

⁴*St. Petersburg State University, Universitetskij pr. 28, 198504 St. Petersburg, Stary Peterhof, Russia*

⁵*Central (Pulkovo) Astronomical Observatory of RAS, Pulkovskoye Chaussee 65/1, 196140 St. Petersburg, Russia*

Accepted XXX. Received YYY; in original form ZZZ

ABSTRACT

A significant part of barred disc galaxies exhibits boxy/peanut-shaped structures (B/PS bulges) at high inclinations. Another structure also associated with the bar is a barlens, often observed in galaxies in a position close to face-on. At this viewing angle, special kinematic tests are required to detect a 3D extension of the bars in the vertical direction (B/PS bulges). We use four pure N -body models of galaxies with B/PS bulges, which have different bar morphology from bars with barlenses to the so-called face-on peanut bars. We analyse the kinematics of our models to establish how the structural features of B/PS bulges manifest themselves in the kinematics for galaxies at intermediate inclinations and whether these features are related to the barlenses. We apply the dissection of the bar into different orbital groups to determine which of them are responsible for the features of the LOSVD (line-of-sight velocity distribution), i.e., for the deep minima of the h_4 parameter along the major axis of the bar. As a result, we claim that for our models at the face-on position, the kinematic signatures of a ‘peanut’ indeed track the vertical density distribution features. We conclude that orbits responsible for such kinematic signatures differ from model to model. We pay special attention to the barlens model. We show that orbits assembled into barlens are not responsible for the kinematic signatures of B/PS bulges. The results presented in this work are applicable to the interpretation of IFU observations of real galaxies.

Key words: methods: numerical – galaxies: evolution – galaxies: kinematics and dynamics – galaxies: structure

1 INTRODUCTION

The barlens component has been introduced only recently in morphological classifications of nearly face-on galaxies. It is described as a new type of lens embedded into the bar and covering about half its length (Laurikainen et al. 2011). Its outline is circular-like, while its azimuth-averaged profile is exponential, which distinguishes barlenses from classical bulges (Laurikainen & Salo 2017; Athanassoula et al. 2015). The barlenses are typically four times larger than nuclear discs and rings and are also distinct from standard lenses (Kormendy 1979) because they are smaller than bars (Laurikainen et al. 2018; Athanassoula et al. 2015).

The so-called B/PS (boxy/peanut-shaped) bulges are also associated with the bars and stand out well against the edge-on stellar disc background (Lütticke et al. 2000a). B/PS bulges are the thickest inner parts of the bars, which have grown vertically as the bars have evolved (Combes & Sanders 1981; Athanassoula 2016; Laurikainen & Salo 2016). Although B/PS structures in N -body

simulations inevitably form as parts of bars (Combes & Sanders 1981), the relationship between B/PS structures and bars is not obvious in observations due to different viewing conditions. This connection is established through the statistics of large samples of galaxies. Lütticke et al. (2000a) (see also Li et al. 2017; Erwin & Debattista 2017) found that up to 45% of all S0-Sd galaxies have B/PS structures, which is close to the fraction of barred galaxies (~ 50%-60%, Marinova & Jogee 2007). Erwin & Debattista (2013, 2017) found that B/PS features extend from 1/3 to 2/3 of the bar radius. In addition to the statistical arguments, kinematic arguments also work: in edge-on galaxies with B/PS structures, traces of a bar can be found from the kinematic characteristics of elongated orbits (Bureau & Athanassoula 2005; Iannuzzi & Athanassoula 2015).

Thus, two structural features of galaxies, B/PS bulges and barlenses, are closely associated with bars. B/PS bulges stand out when the galaxy is viewed edge-on, and barlenses are well identified visually when the galaxy is positioned almost face-on. That is why the idea has recently spread that ‘barlens’ and ‘box/peanut’ are the same stellar structure, namely the inner part of the bar, but seen at different viewing angles (Laurikainen et al. 2014; Athanassoula 2016). The

* E-mail: dzakharovaa@gmail.com

identification of the two structures was based on several arguments, mostly indirect. The parent galaxies of barlenses and B/PS structures have a similar total stellar mass distribution (Laurikainen et al. 2014). Relative to the bar, barlenses have similar sizes (Athanasoula et al. 2015) as obtained for the B/PS bulges by Lütticke et al. (2000b) and Erwin & Debattista (2013). However, the main evidence came from analysing the results of N -body simulations. By viewing their snapshots from many different angles, Athanassoula et al. (2015) concluded that barlenses are simply the vertically thick part of the bar, i.e., the barlenses in the edge-on position appear as B/PS bulges. Stronger evidence comes from an analysis of the kinematics of galaxies with barlenses. First, Méndez-Abreu et al. (2008) found kinematic evidence of the B/PS bulge for the galaxy NGC 98 classified as having a barlens (Laurikainen & Salo 2017). Then, for NGC 1640, which classified as a galaxy with a barlens (Laurikainen & Salo 2017), Méndez-Abreu et al. (2014) showed a kinematic hint of the presence of a B/PS bulge in the central regions of the bar. Finally, the TIMER team (Gadotti et al. 2020) claim to have found in the barlens region of several nearly face-on galaxies kinematic signatures of both a bar and a box/peanut, as expected from numerical simulations. But for almost face-on galaxies it is not yet clear which structural component of the bar (the bar itself or the barlens) is associated with the discovered kinematic signatures of a ‘peanut’. That is why even the kinematic data needs a more accurate interpretation.

This question can be solved using the results of the orbital analysis of numerical models. Recently Tikhonenko et al. (2021) have dissected a bar in one typical N -body model with a barlens into separate orbital components supported by completely different types of orbits. This work shows that the part of the barlens with rounded isophotes in the face-on view is a rather flat structure in the vertical direction without any significant off-centre protrusions and signatures of a peanut. It was also concluded that the edge-on B/PS bulge is a barlens-independent component of the bar and is supported by various types of orbits. One can not separate the face-on image of the galaxy into individual orbital components and find kinematic parameters for these components, but by using the results of N -body simulations and orbital analysis, one can understand which orbital subsystem contributes to the kinematic features of a peanut.

Four parameters are often used in kinematic diagnostics: the mean velocity \bar{V} , the velocity dispersion σ , and h_3 , h_4 parameters, which measure the deviations of the LOSVD (line-of-sight velocity distribution) from a Gaussian. The last two parameters are the corresponding coefficients that arise when the velocity profile is expanded by orthogonal Gauss-Hermite functions. The parameter h_3 measures asymmetric deviations from the Gaussian, while the parameter h_4 measures symmetric ones. These deviations occur when different velocity components on the line of sight do not contribute equally to the LOSVD (van der Marel & Franx 1993; Gerhard 1993).

Debattista et al. (2005) used kinematic diagnostic to analyse the LOSVD of barred face-on galaxies. In this case, there is a single velocity component, a vertical one (v_z). Debattista et al. (2005) noted that the velocity distribution (VD) for the vertical component $f(v_z)$ may differ from the Gaussian and lead to negative values of h_4 if the density distribution in the vertical direction is flat-topped, i.e., not so strongly concentrated towards the mid-plane compared to the surrounding disc. The flat-topped volume density distribution in the vertical direction is expressed in terms of negative values of the fourth coefficient of Gauss-Hermite expansions d_4 (an analogue of h_4). It opens up the possibility of confirming the relationship between bars (structures that are well identified in a nearly face-

on view) and B/PS bulges, which are seen predominantly edge-on. Debattista et al. (2005) have noticed that negative values of h_4 along the major axis of the bar at inclinations less than 30° indicate the presence of the peanut if they form two deep minima on both sides of the centre of the galaxy. Two shallow minima of h_4 along the major axis of the bar indicate not a peanut, but a contamination of the LOSVD by other velocity components, in addition to v_z .

The origin of the negative h_4 values is still not clearly understood while being particularly important in the light of recent high resolution integral field unit (IFU) spectroscopy data (for instance, the TIMER project, Gadotti et al. 2019). The accurate interpretation of these features (negative h_4 values) would require a set of synthetic 2D maps of the common kinematic parameters (\bar{V} , σ and h_3 , h_4 parameters) based on a wide grid of numerical models viewed from different inclinations and bar major axis viewing angles.

We intend to explore model kinematic maps for intermediate inclinations, thus extending the data available from Debattista et al. (2005) for a face-on view and from Iannuzzi & Athanassoula (2015) for mainly high inclined models. In addition, since quite a lot of galaxies with barlenses fall into the sample by Gadotti et al. (2020), we would like to conduct a comparative analysis of 2D maps for models with gradually changing bar morphology from models with barlenses to models without features in the face-on structure of the bar. We also intend to collect the analysed model data into data cubes with an appropriate spectral resolution for the most plausible comparison with observational data cubes. Such maps will be useful both for interpreting existing and future observational data. Since 2D kinematic maps for inclined galaxies can differ from face-on maps, it is necessary to extend the analysis of the LOSVD distortions due to i) density distribution features, ii) contamination of the LOSVD by various velocity components. This will help to better understand the relationship of kinematic parameters and B/PS bulges in cases when the B/PS bulges themselves are not visible. Finally, having the results of an orbital analysis for a number of numerical models, we have a unique opportunity to study the influence of different orbital groups on the kinematic picture and to understand which orbital groups (assembled into a barlens or into the bar itself) raise distortions into the LOSVD and create peanut signatures when the galaxy is viewed face-on.

In this article, we focus only on the features of the LOSVD, which are measured by the parameter h_4 . We leave the joint analysis of the parameters h_3 and h_4 for future works.

The paper is organised as follows. In Section 2, we describe our N -body models as well as our dissection of the models into various orbital groups assembled into different sub-structures of the bar, explain how we prepare data cubes for all models and for a set of inclinations and position angles of a bar and discuss how we extract the main kinematic parameters from LOSVDs in each pixel. In Section 3, we present our results, compare 2D kinematic maps for models with a barlens and with an ordinary bar at face-on view and other positions of a bar. In Section 4, we differentiate the effects of a flat-topped vertical density distribution and effects of inclinations associated with contamination of the LOSVD by velocity components other than v_z . In Section 5, we focus on the contributions of different orbital groups into features of the LOSVD. In Section 6 we discuss the astrophysical applications of our results. In Section 7, we give our conclusions.

2 DATA PREPARATION

2.1 N-body models

To study the kinematic properties of B/PS bulges, we use a set of self-consistent pure N -body (i.e., without the gas component) models from Smirnov et al. (2021). In the following description and most of the illustrations, we adopt the unit system where 1 length unit is equal to 3.5 kpc, $G = 1$, and unit mass is equal to $5 \times 10^{10} M_{\odot}$. Assuming these values, a time unit would be equal to 13.8 Myr.

The initial conditions for each model were prepared with `mk-galaxy` script (McMillan & Dehnen 2007). At the start of simulations, all models have a stellar disc embedded into a self-consistent (“live”) dark halo.

The stellar disc of each model has an exponential radial profile and is isothermal in the vertical direction:

$$\rho_d(R, z) = \frac{M_d}{4\pi R_d^2 z_d} \cdot \exp(-R/R_d) \cdot \text{sech}^2(z/z_d), \quad (1)$$

where R is the cylindrical radius, $M_d = 1$ is the total mass of the disc, $R_d = 1$ and $z_d = 0.05$ are scale lengths in radial and vertical directions, respectively.

The halos are spherical and have Navarro-Frenk-White-like (Navarro et al. 1996) profile with dark matter mass for each model equal to $M_h(r < 4R_d)/M_d \approx 1.5$.

For three models, a spherical Hernquist bulge (Hernquist 1990) in the central area was added. All models in the course of their evolution develop bars with B/PS bulges and X-structures (the brightest part of the B/PS bulges) visible at the edge-on position. We distinguish models by their nicknames according to the final morphology of their bars: BL (BarLens), BLx (BarLens + slight traces of face-on X-shaped bar), Xb (face-on X-shaped bar + bulge), X (face-on X-shaped bar). BL and BLx models are the galaxies with a barlens in a face-on position (first and second columns in Fig. 1). X and Xb models represent galaxies with X-shaped (or peanut-shaped) bars in a face-on position (third and fourth columns in Fig. 1). Such a morphology difference is due to the presence/absence of the bulge. The bulges in models differ in the total mass M_b and radial scale lengths r_b (Table 1).¹

Each subsystem was represented by a specific number of “star”-particles: 4×10^6 for the disc, 4.5×10^6 for the halo. The total number of bulge particles is determined according to the value of the ratio M_b/M_d , with a reference point for the Xb model, where the number is equal to 0.8×10^6 .

The disc radial dispersion profile was exponential with $\sigma_R = \sigma_0 \cdot \exp(-R/2R_d)$, where σ_0 is a normalisation constant. It is inferred from the Toomre parameter value: $Q(2R_d) = Q_0$ with Q_0 set to 1.2. Thus, we consider a marginally stable stellar disc. The evolution of all models was traced by `gyfacc10N` integrator (Dehnen 2002) from the NEMO suite (Teuben 1995) for approximately 8 Gyr with 1.7 Myr time step. Fig. 1 shows snapshots for our models for $t = 450$ (≈ 6.2 Gyr).

The key difference between the models is their initial bulge concentration, which results in different gradient of the rotation curve in the centre. For example, the BL model has the steepest rotation curve in the central regions (see Smirnov et al. 2021, figure 1). The relation between the slope of the rotation curve in the inner parts of the galaxy and different face-on bar morphology was first noted by (Salo & Laurikainen 2017). Our BL model does fall into the range

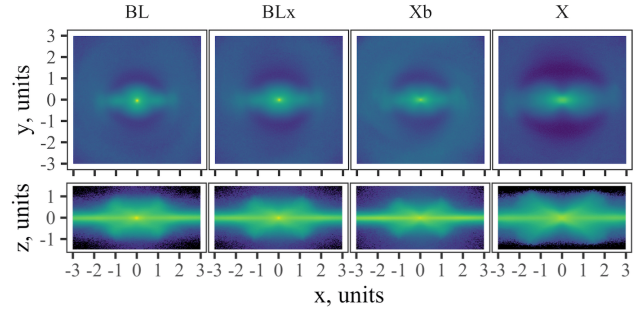


Figure 1. The set of models (BL, BLx, Xb, and X) from Smirnov et al. (2021) used in this work. The *top* row shows face-on views of the corresponding model in $(x, y) = [-3; 3] \times [-3; 3]$ area, while the *bottom* row displays edge-on views in $(x, z) = [-3; 3] \times [-1.5; 1.5]$.

model	X	Xb	BLx	BL
M_b	0	0.2	0.1	0.1
r_b	-	0.2	0.1	0.05

Table 1. The properties of classical bulges in our models, see text for the adopted unit system description.

of parameters for which the model develops a clear barlens. Thus, the chosen setup of models yields a gradual progression in face-on bar morphology from a bar with a barlens to a face-on peanut, which makes this model set optimal for understanding the nature of the barlens and its connection with a B/PS bulge: either in terms of its vertical structure (done in Tikhonenko et al. 2021) or its kinematics (this work).

2.2 Orbital groups

In Parul et al. (2020) and Smirnov et al. (2021), the entire orbital structure of several self-consistent N -body models with bars were analysed using Fourier analysis of spatial coordinates of each star-particle. Four models presented in Section 2.1 fall into the grid of models for which orbital analysis was performed. Thus, we have unique data for studying the kinematics of individual orbital groups and searching for kinematic signatures of a peanut on face-on snapshots that we can attribute to one or another orbital group.

The conducted orbital analysis is based on spectral dynamics methods (Binney & Spergel 1982). For all orbits in the disc, the Cartesian frequencies (f_x , f_y , and f_z) in the rotating coordinate frame with x -axis aligned with the bar major axis² have been computed by finding the position of the highest peaks in Fourier spectra of the corresponding Cartesian coordinates are x , y , z .

In addition to f_x , f_y , and f_z , we have determined the radial oscillations frequency f_R . Thus, a set of four numbers for every orbit in a disc for each model have been obtained. Using the ratios of these frequencies f_x/f_R and f_y/f_R , Smirnov et al. (2021) found several orbital groups in their grid of models. These orbital groups assemble in specific structures, and a dominant group or a combination of groups are responsible for a particular morphological feature of a model bar. Thus, the bar can be disassembled into the following orbital groups.

¹ One should bear in mind that galaxies which show X-shape at low inclinations are quite rare.

² To identify the bar major axis we diagonalise the moment-of-inertia tensor of a subset of particles ($R < 0.8$, $|z| < 0.3$) and find principal axes.

orbital group	X	Xb	BLx	BL
x1+x2+x4	3.79	6.52	9.51	11.35
boxy bar	45.19	25.68	23.88	10.45
bl _o	5.36	7.82	9.98	13.49
bl _u	0.96	1.05	3.42	9.22

Table 2. The percentage of orbits of each type in the models. The fraction (%) is given relative to the total number of particles in the disc (4×10^6).

- A so-called ‘classic’ bar, identified by the condition $f_R/f_x = 2.0 \pm 0.1$. This orbital group primarily consists of loop orbits with $f_y/f_x = 1 \pm 0.1$ (in the sense of the orbital classification by Valluri et al. 2016) with x1-like and x2-like (prograde) or x4-like (retrograde) orbits being the prominent members of it. An x1-like family gives a narrow and elongated bar with an inner bar-like structure superimposed on an outer bar and oriented perpendicular to it (x2-like or x4-like orbits).

- Boxy orbits, selected via criterion $f_R/f_x = 2.0 \pm 0.1$ and $f_y/f_x > 1.1$. These orbits constitute a face-on peanut, or the so called ‘boxy bar’, and are part of the extended bar.

- Two non-classical groups: bl_o and bl_u in notation of Smirnov et al. (2021). Orbits from these two groups have f_R/f_x either larger than 2 (bl_o) or smaller than 2 (bl_u). They are definitely not from the outer disc, but at the same time they are not quite elongated with the bar and do not precess synchronously with it. These orbits have rather complex frequency proportions. Orbits from the bl_u family have $f_y/f_x = 1.0$. As to the orbits from the bl_o family, they split into two branches, with $f_y/f_x = 1.0$ (more extended structure) and with $(f_y + f_x)/f_R = 1.0$ (more compact structure). All this gives them the overall ‘roundish’ shape, which results in the formation of a barlens in the N -body model that has it. The bl_u orbital group is a key component of a barlens and maintains the rounded shape in the central area of the bar. The bl_o orbits are assembled into a more extended square-like structure, which is nevertheless a part of the barlens.

The percentage of orbits of each type in the models is compiled in Table 2.

One of the main conclusions made by Smirnov et al. (2021) is that the dominance of one or another orbital group determines the face-on morphology of a bar and its features. In Section 5, we use the data on the bar orbital groups revealed in Smirnov et al. (2021) to determine their contribution to pixels with peanut signatures at the face-on position of the galaxy.

2.3 Databucubes

To study kinematics, one needs to represent the velocities of model particles in a way that can be faithfully compared with observational data. The most common form of data used in kinematic studies is a databucube. Here, we construct synthetic databucubes from our simulations.

The best stellar kinematics available to date were obtained by TIMER project (Gadotti et al. 2019), conducted on the MUSE spectrograph on the VLT. The high-level products of their processing pipeline are the maps with stellar kinematics parameters, which are publicly available on the TIMER website³. We use these maps as

a reference point for the construction of our synthetic maps. We model our databucubes to have a comparable spatial resolution to MUSE. Specifically, we assume the whole image to be $30' \times 30'$ and the pixel size of each slice to be $300\text{px} \times 300\text{px}$. The proper choice of the spectral axis was more arbitrary. Normally, the velocities from integral-field spectroscopy (IFS) data are inferred via advanced pipelines, such as GIST (Bittner et al. 2019), which in turn uses pPXF (Cappellari & Emsellem 2004) for stellar kinematics. These pipelines estimate the LOSVD by fitting a linear combination of template library spectra to the real spectrum of the galaxy. However, in case of our N -body models, a realistic imitation of stellar spectra would be unnecessary complex for the task at hand. Instead, we take the mean velocity uncertainty from (Bittner et al. 2019), where it was estimated to be $\approx 5\text{km s}^{-1}$, and assume the same uncertainty for the positions of the LOSVD bins. Thus, we simply assume the bin width to be equal to $2\sigma \approx 10\text{km/s}$.

To improve signal-to-noise⁴ ratio (S/N) of the final databucubes, we stack 17 snapshots in the time interval $t = 448 - 452$. During this period by $\Delta t = 4$, the change in the bar pattern speed is insignificant (see Figure 2 in Smirnov et al. 2021). Thus, 74.8 million particles in total are reached. Contrary to the similar procedure in Iannuzzi & Athanassoula (2015) we do not enforce any kind of symmetry to the model along the principal axes of the bar, because the total number of particles was already sufficient for the purposes of this paper after stacking.

To obtain the line-of-sight velocities, we rotate the model to match its z -axis, initially perpendicular to the disc plane, with the chosen direction of the line-of-sight and project the full velocity (v) on the new z -axis. Then, the velocity is binned from $\min v_{\text{LOS}}$ to $\max v_{\text{LOS}}$ with the bin width equal to the velocity resolution assumed above. In addition to that, we also compute the LOS projections of the vertical (v_z), azimuthal (v_φ), and radial (v_R) velocity components in the *original* coordinate frame. Thus, for every spatial pixel of the databucube, we effectively have four distributions: one of the total LOS velocity and three distributions of the LOS velocity components. In practice, we just made a dedicated databucube for each velocity component to simplify the further processing.

In a similar fashion, for each model we prepare the set of databucubes excluding each orbital family one-by-one. In Section 5, we would use these databucubes to estimate the contributions of orbital groups in LOSVDs of databucubes. This approach was chosen instead of considering each component alone, because it results in databucubes with a larger number of particles that are easier to analyse and to compare with observational data.

We deliberately do not apply the Voronoi-binning technique, which is quite common in similar studies, because in this case it is harder to compare our databucubes for different models fiber-by-fiber (our Section 3) as well as different velocity components for the same model (Section 4). In addition to that, it is rather unclear how to study the effect of individual orbital groups (our Section 5), because the tessellation should be again different for every databucube and the additive property of LOSVD in a given fiber can no longer be used. For the same reasons, we also do not smooth the layers of the databucubes with the instrumental PSF.

⁴ In absence of real errors, we assume an artificial noise with Poisson distribution, thus S/N scales as $N^{-1/2}$.

³ <https://www.muse-timer.org>

2.4 Determination of kinematic parameters

To describe deviations from the Gaussian profile, line-of-sight velocity distributions of galaxies are often represented by a product of its Gaussian and non-Gaussian parts. The latter term is further expanded into Gauss-Hermit series (van der Marel & Franx 1993; Gerhard 1993), resulting in the following expression for the overall profile:

$$\mathcal{L}(v) = I \frac{1}{\sqrt{2\pi}} e^{-w^2/2} \cdot \sum_{j=0}^N h_j H_j(w), \quad w = \frac{v - \bar{V}}{\sigma}, \quad (2)$$

where I is a normalization constant (corresponding to the intensity), \bar{V} is a mean velocity, σ is a velocity dispersion, $H_j(w)$ are Hermite polynomials, and h_j are coefficient (or factors) of Gauss-Hermit series.

The most commonly used parameters in kinematic studies apart from the mean velocity and its dispersion are h_3 and h_4 , which tell about the ‘skewness’ and the ‘broadness’ of the distribution respectively. The values of these parameters can be estimated in different ways. One approach would be to use the orthogonality property of Hermit polynomials and compute the factors directly via the corresponding scalar products (see Debattista et al. 2005 for an example of its application). However, in this work, we follow van der Marel & Franx (1993); Brown et al. (2013) and Iannuzzi & Athanassoula (2015), and simultaneously obtain the values for all free parameters (I , \bar{V} , σ , h_3 , and h_4). This approach was chosen to ease the comparison with previous studies and for performance reasons. Thus, we truncate the series up to the fourth order to avoid overfitting to noise and effectively fit the profiles with the following function:

$$\mathcal{L}(v) = I \frac{1}{\sqrt{2\pi}} e^{-w^2/2} \left(1 + h_3 H_3(w) + h_4 H_4(w) \right), \quad w = \frac{v - \bar{V}}{\sigma}. \quad (3)$$

In the case of a nearly Gaussian distribution, h_3 and h_4 parameters are around zero. However, if the system is dominated by radial orbits, the distribution becomes narrower compared to the Gaussian and the fit would produce positive values of h_4 . If the system has predominantly circular orbits, then the distribution broadens. In this case, one measures the negative values of h_4 (Gerhard 1993; van der Marel & Franx 1993). Negative values of h_4 may also appear when the LOSVD is a sum of two Gaussians with clear double-peaked structure, which is typical for two subsystems with different average rotation speeds (Gerhard 1993).

Using the fitting procedure described above⁵ (Eq. (3)), we obtain an intensity, mean velocity and its dispersion, and h_3 and h_4 map for each synthetic datacube. To characterise the density distribution, we calculate the d_4 parameter in a similar way using Eq. (4)

$$\mathcal{L}(z) = \mu_0 \frac{1}{\sqrt{2\pi}} e^{-\psi^2/2} \left(1 + d_3 H_3(\psi) + d_4 H_4(\psi) \right), \quad \psi = \frac{\mu_1 - z}{\mu_2} \quad (4)$$

with $(\mu_0, \mu_1, \mu_2, d_3, d_4)$ being the free parameters of the fit.

3 LOSVD MOMENT MAPS

For galaxies with a B/PS bulge, the density distribution in the vertical direction in the area of the B/PS bulge differs from the usual

exponential distribution or the distribution characteristic of a self-gravitating isothermal layer (see Eq. (1)). The density distribution is more vertically extended than the surrounding disc, i.e., the thickest parts of the bars are very loose, and the parameter d_4 in Eq. (4) becomes negative. In this section, we follow the approach of Debattista et al. (2005) and explore the connection between vertical density features (d_4) and the thickness with the kinematics (h_4) for different inclinations of the model and different bar position angles.

3.1 Face-on maps

Fig. 2 (upper row) demonstrates 2D maps of the parameter h_4 for our models (BL, BLx, Xb, and X). We obtained h_4 values for each pixel constituting the face-on snapshots of models as described in Section 2.4. The h_4 maps for prepared models have different morphology for the face-on case due to the different morphology of the bar.

Regardless of the type of the B/PS bulge, for all modelled maps there are negative values of h_4 within the bar radii (Fig. 2). The cuts along the major axis also display the double-sided minima as discussed in Debattista et al. (2005). Although, we note that the difference between these h_4 maps depends on the exact morphology of the model. For the BL model, the minima of the h_4 parameter lie outside the rounded central isophotes, and the pixels with negative values of h_4 are grouped mainly on the major axis of the bar. At the same time, for BLx, Xb, and X models, the negative values of h_4 parameter draw an area that looks like a ‘bow tie’. In the particular case of the model X, which has the largest B/PS bulge of all of the models, the negative values of the parameter h_4 still lie close to the site occupied by the face-on peanut-shaped bar, while the morphology of the h_4 maps reflects the X-shaped morphology of its bar (compare Fig. 1 and Fig. 2).

Using cuts along the major axis of the bar (Fig. 3, solid lines), we show the values of the h_4 parameter along the major axis for all models. In Fig. 2 (upper row) the position of h_4 minimum is shown by a vertical line and its location is indicated in the dimensionless units of this work. In all models, the minimum values of h_4 are similar and equal to -0.05 . However, the minimum of h_4 along the major axis of the bar is reached at different distances from the centre. For the BL and BLx models, the h_4 minimum along the major axis coincides with the boundary of inner rounded isophotes where the transition to a narrow extended bar occurs. Xb and X models have their h_4 minima along the major axis closer to the centre of the galaxy than the BL and BLx models, but they are wide (especially for the X model). This is clearly seen on the profiles of the h_4 parameter along the major axis of the bar (Fig. 3). If we compare the position of the negative minima of the parameter h_4 on the major axis with the dimensions of the B/PS bulge, as it is seen on the side-on snapshots (Fig. 1), then they do not match. B/PS bulge is larger. At the same time, the maps in the Fig. 2 (upper row) show that negative values of the h_4 parameter are present not only along the major axis of the bar, but are also partially localized in the bar itself away the minima on the major axis along four rays. The rays roughly outline the dimensions of the B/PS bulge.

We also checked the relationship between the flat-topped distribution of the LOSV (measured by h_4) and the features of the vertical density distribution (d_4), as well as between h_4 and the thickness for all our models. To measure the thickness, we calculate the median value of absolute distance to the disc plane (hereinafter, $\text{med}|z|$) for all particles that create a signal in a given pixel. We also computed d_4 using Eq. (4). The middle and bottom rows in Fig. 2 show the d_4 and $\text{med}|z|$, respectively, for all our models. Re-

⁵ We additionally checked the fitting results with the MCMC parameter estimation and found no significant deviations from the former method, which is much faster.

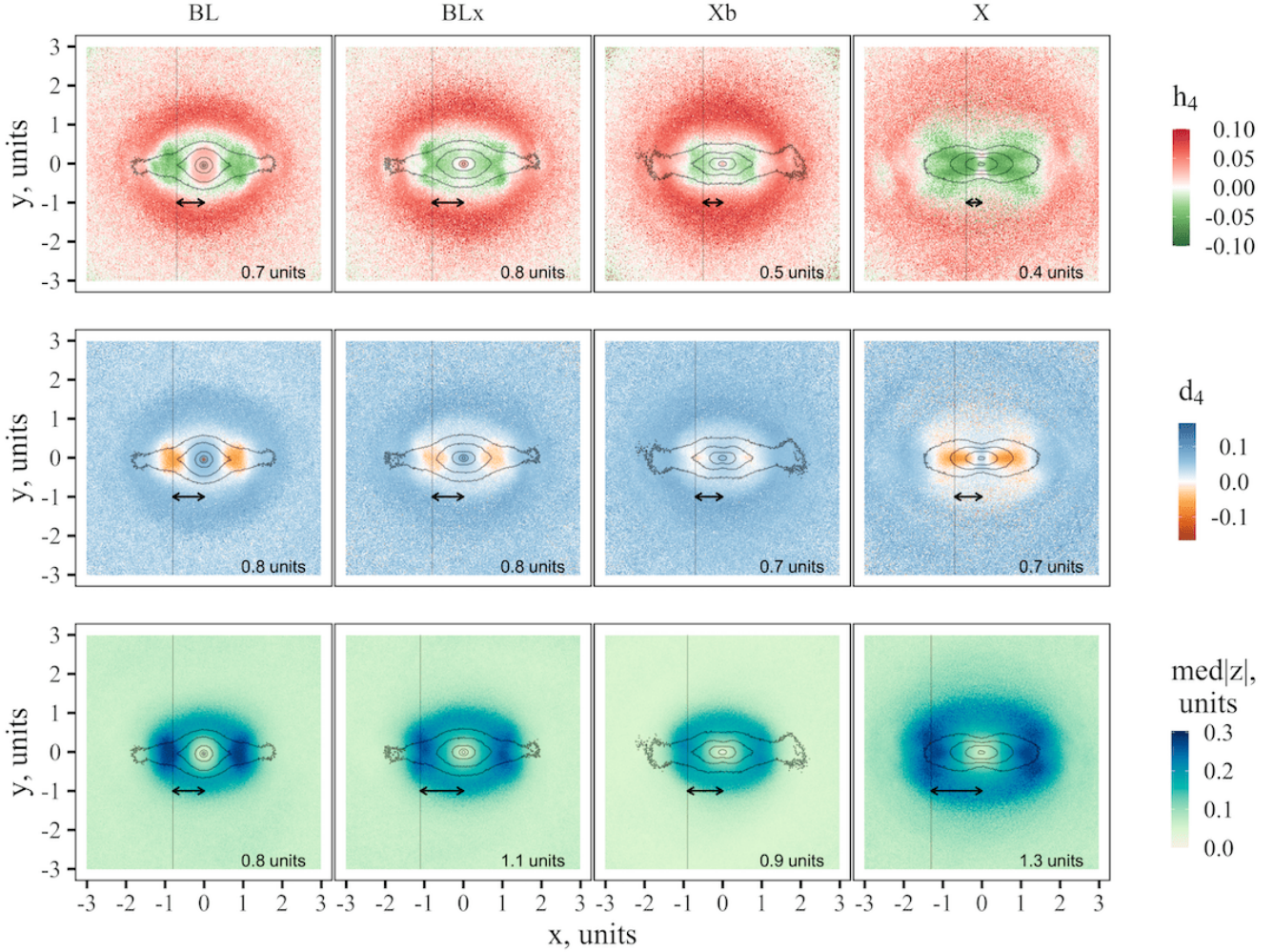


Figure 2. 2D maps of the h_4 parameter (upper row), the vertical density distribution parameter d_4 (middle row) and the $\text{med}|z|$ (bottom row) for all model galaxies at face-on position ($i = 0^\circ$, $\text{PA} = 0^\circ$). The isophotes for each model correspond to the intensity maps shown in Fig. 1. The vertical lines define the position of the h_4 and d_4 minima and the maximum of thickness ($\text{med}|z|$) along the major axis of the bar (the exact values of the distance from the centre of the model galaxy to the extremum are indicated at the bottom of the maps).

Regardless of a specific model, all our models have a good correlation between h_4 and d_4 parameters, as galaxies with B/PS bulges. We additionally checked the Pearson correlation coefficient between h_4 and d_4 along the major axis. For our models, it varies from 0.79 to 0.83.

The Xb model is a little out of the general range of models. It has the loosest and most massive classical bulge. In the area of the bar and at the face-on position, the bulge particles through which the line of sight passes blur the features of the vertical density distribution of the B/PS bulge, which, for this reason, hardly appear on the d_4 map (Fig. 2, middle row). At the same time, B/PS bulge signatures are still visible on the kinematic maps (h_4 maps, Fig. 2, upper row), and green pixels (negative values) are located along the bar up to the boundaries of the B/PS bulge, as seen edge-on (Fig. 1).

Thus, the flat-topped vertical density distribution can be traced from the flat-topped LOSVD distribution for face-on galaxies. In the following sections, we discuss the limitations of this approach.

The relationship between h_4 and the thickness ($\text{med}|z|$) of the B/PS bulge is shown in Fig. 2 (upper and bottom rows). We have

obtained a formal match between the minima of the h_4 parameter and the thickness only for the BL model. For all other B/PS bulge models, the h_4 parameter does not trace the thickness. Thus, the parameter h_4 is only an indicator of features of the vertical density distribution, but not the thickness.

3.2 Inclination effects for h_4 maps

In this subsection, we explore in detail how the h_4 maps change depending on the galaxy inclination and the position angle (PA) of the bar major axis relative to the line of nodes. We also discuss the absence of connection between h_4 and d_4 when the model is inclined. We now focus only on the BL model, since all other models behave in a similar way. The corresponding figures for BLx, Xb, and X model can be found in Appendix A. In Fig. 4 we present the changes of h_4 maps varying both inclination angles (0° , 20° , 40° , 60°) and position angles (0° , 45° , 90°) of the bar. This set of observer positions broadly covers all relevant options. We additionally

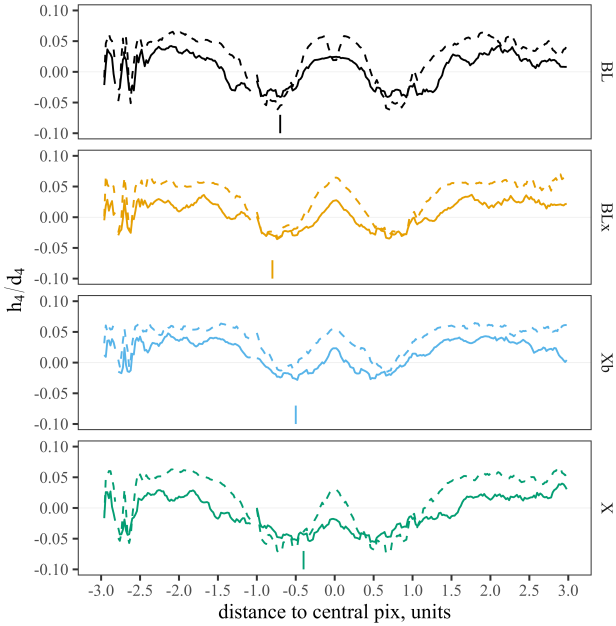


Figure 3. The h_4 (solid lines) and d_4 (dashed lines) profiles along the major axis for the BL, BLx, Xb, and X models. The short vertical bars at the bottom of the plots indicate the position of the h_4 minima and correspond to the vertical lines in Fig. 2 (upper row).

add inset plots with d_4 maps to the upper right corner of each panel with h_4 maps.

The leftmost columns of Fig. 4 show h_4 (main panels) and d_4 (inset panels) parameters for different inclinations with $PA = 0^\circ$. The parameter d_4 stops being a reliable vertical density distribution indicator with the inclination of a model galaxy even if the position angle is close to zero. It happens because particles at different distances from the center of the galaxy end up in the same line of sight. Respectively, the connection between h_4 and d_4 is broken. The reason is the contamination of v_z by other velocity components (we discuss it in detail in Sec. 4). This is especially well seen on the h_4 and d_4 profiles along the major axis of a bar (Fig. 5), where the h_4 parameter along the major axis behaves in a different way than the d_4 . The inclination of the galaxy moves the minima of h_4 away from the galaxy center. Also, for inclined galaxies ($i \gtrsim 20^\circ$), the h_4 minima become less prominent. We support this statement by the cuts along the major axis for the BL model in Fig. 5.

The same tendency to move the minimum of h_4 to the periphery along the major axis with increasing inclination is also observed when the inclined galaxy has a non-zero position angle. The second and the third columns of Fig. 4 show the h_4 for $PA = 45^\circ$ and $PA = 90^\circ$ respectively. The prominent two-sided h_4 minima along the major axis create a semi-closed ‘ring’ of negative values already at $PA = 45^\circ$ and closed ‘ring’ at $PA = 90^\circ$. Maps with $i \approx 40^\circ$ – 60° look very disturbed and the deepness of h_4 minima on the line of nodes increases (Fig. 5). A change of the PA for an inclined galaxy also increases the h_4 minima, and creates a prominent ‘ring’⁶ of h_4 minima. Moreover, such a ring is typical not only for the model with barlens (BL) but also for all the others (Fig. A1, A2, A3).

⁶ Signatures of a ring from negative values of h_4 can be noticed in figure 29 by Iannuzzi & Athanassoula (2015) (the case $PA = 90^\circ$, $i = 60^\circ$, models GTR101 and GTR116, which have barlenses).

When $PA = 0^\circ$ and $i \geq 40^\circ$, the minima of h_4 lie on the major axis of the bar, and the minima of d_4 form two arcs symmetrically crossing the minor axis. At the same time, for $PA = 90^\circ$ and $i \geq 40^\circ$, the deepest minima of the parameter h_4 appear along the minor axis, which are not reflected in any way in the minima of the parameter d_4 , although the relationship between the minima can be traced along the major axis. We return to the discussion of these features in Sections 4 and 5.

To conclude this section, we note that the appearance of h_4 maps is affected not only by the actual morphology of the bar but also by the position of the barred galaxy with respect to the observer. We note that for all our models with B/PS bulges, these effects manifest themselves in a similar way. At the same time, for inclined galaxies ($i \geq 20^\circ$), the features of the LOSVD are no longer related to the features of the density distribution in the vertical direction. In the next subsection, we compare all our models at an intermediate inclination in an attempt to better characterise the features of the maps. We also pay attention to the fact that when the galaxy is inclined, the minima move away from the center of the model, and their position can no longer reflect the size of the bar.

3.3 The differences between models on h_4 maps

Many galaxies from the TIMER project (Gadotti et al. 2019) have inclinations in the range $i = 30^\circ - 60^\circ$. So, in this section, we pay special attention to the differences between our models with a significant inclination. Fig. 6 shows the h_4 maps for all models at $i = 40^\circ$ and different position angles $PA = 0^\circ, 45^\circ, 90^\circ$. The first line corresponds to $PA = 0^\circ$ and we do not notice a significant difference between the models BL, BLx, and Xb. Although the map for the model without the bulge (X) differs from the others and the position of its h_4 minimum along the major axis of the bar lies as far as possible from the centre of the galaxy (2.4 units), it does not make it possible to distinguish between the vertical structure of bars of different morphology, i.e., to identify B/PS bulges with certain parts of the bar.

The rotation of the kinematic axis by 45° (second row in Fig. 6) makes the BL, BLx and Xb models even less visually distinguishable. The main difference between the h_4 maps for these models at such position angles is the degree of compactness of the location of the features on the maps: the minimum of h_4 is slightly further from the centre for the BLx model. The differences between the BL and Xb models are completely insignificant, although the Xb model does not contain a barlens. As for the X model, we note that the h_4 maps corresponding to this model differ from the rest only in that the minima are located almost one and a half times farther from the centre of the galaxy (0.9 units versus 0.6), due to the fact that the bar of this model is more extended, as well as its B/PS bulge (cf. Fig. 1).

In the case $PA = 90^\circ$, the map shows the ring of negative values of h_4 for all models, regardless of the existence or absence of a barlens. The main difference between the rings of negative values of h_4 for the BL and X models is their shape (for the X model the ring is more squared) and the size of the ring (for the X model the ring is larger). However, there is practically no difference between the BL, BLx, and Xb models for this position of the galaxy.

Thus, the presence of the ring of negative values of h_4 is not related to the exact bar morphology, but to the inclination effects, which can manifest themselves in two ways. First, at intermediate inclinations, the LOSVD is contaminated by other velocity components, in addition to v_z . Thus, the negative values of h_4 are determined by the contribution of these other components to the

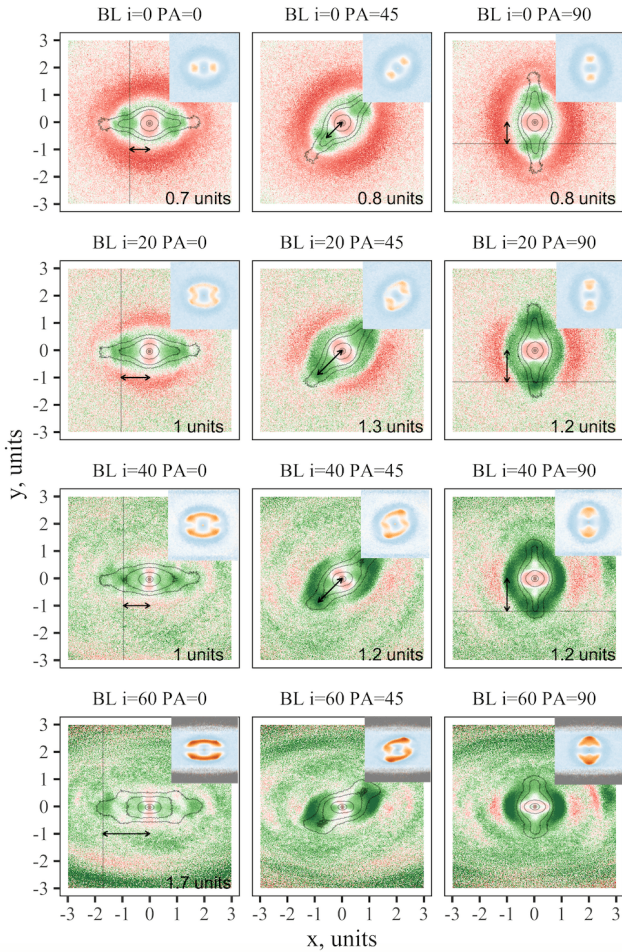


Figure 4. Effects of galaxy inclination (i) and PA in the h_4 maps for the barless model (BL). The isophotes correspond to the intensity maps for a given inclination. Straight lines with arrows show the position of the h_4 minima along the major axis of the bar. The number at the bottom shows the distance from the centre of the model galaxy to the h_4 minimum along the major axis. For $i = 60^\circ$ and PA = 45°, 90° the positions of the minima are not indicated since there are no global minima along the major axis. In the upper right corner of each panel, the insets with d_4 corresponding to the given position of the galaxy are added. The colors are the same as in Fig. 2. The minima of h_4 are broad. Therefore, the precise location of exact global minima is not very well defined and may slightly differ for different viewing angles even in case of $i = 0^\circ$.

LOSVD and their features, and not by the looseness of the density distribution. Second, stars with other kinematics, different from the kinematics of the stars of the bar or any of its subsystems, may appear on the line of sight. Even if the VD for individual subsystems is close to a Gaussian, the sum of Gaussians with different mean velocities can lead to the effect of negative values of h_4 (Gerhard 1993).

4 CONTAMINATION OF THE LOSVD BY DIFFERENT VELOCITY COMPONENTS

In Section 3, we only discussed how the h_4 maps generally change for our four models depending on the bar morphology, inclination,

and position angle of a bar major axis relative to the line of nodes. In this section, our goal is to explain why the location of negative h_4 minima for our BL model shifts on the maps depending on the inclination and position angle. To do this, we consider only the BL model and separate the velocity components in each cube since now. In contrast to the face-on position, for inclined galaxy, the LOSVDs can contain contributions from both v_φ and v_R in addition to v_z . These velocity components distort the LOSVD, although they have nothing to do with the flat-topped density distribution in the vertical direction.

4.1 Contamination of LOSVD by azimuthal velocity component

Our first example is a pixel on the bar major axis for the BL model, at the distance of 1.7 units from the centre (Fig. 7, upper right plot, a cross). In this pixel, particles with different z , but with the nearly same values of $y = 0$ (for $i = 0^\circ$), fall on the line of sight (Fig. 8, left plot, light grey line). In the face-on position, when only the vertical component of the velocity v_z contributes to the LOSVD, the value of h_4 in this pixel is positive (Fig. 5, upper left cut, solid line and Fig. 7, upper right plot, a cross in red region), and the distribution function $f(v_z)$, in contrast to the Gaussian, has a sharp peak (Fig. 7, upper left plot). This is in good agreement with the density distribution in the vertical direction, which also has a narrow peak (Fig. 7, upper middle plot).

When the stellar disc is inclined around the major axis of the bar at an angle $i = 60^\circ$, the distance from this pixel to the centre of the disc does not change (Fig. 7, bottom right plot, a cross). At the same time, the line of sight in this case captures particles not only with different z but also with different y (Fig. 8, left plot, orange line). Now, not only the vertical velocity component v_z (green line on the bottom left panel of Fig. 7), but also the azimuthal one (cyan line), contributes to the LOSVD in this pixel, and the LOSVD (dark blue line) is characterised by a negative value of h_4 (Fig. 7, bottom right plot, a cross in green area). Moreover, in this pixel, there is a negative minimum of h_4 , which was not in this place for the model in the face-on position (Fig. 5, left cuts, solid lines). The LOSVD in this pixel is flat-topped (Fig. 7, bottom left plot) but its shape is determined mainly by $f(v_\varphi)$ because $f(v_z)$ in this pixel is narrow peak around zero, which means that the projection of the v_z on the LOS is rather small. We know that it is the shape of the distribution function $f(v_z)$ that is related to the features of the density distribution in the vertical direction, i.e., only a flat-topped $f(v_z)$, which gives a negative value of h_4 , implies a flat-topped density distribution. Thus, it is impossible to conclude that this pixel shows the signatures of a peanut. This is confirmed by the density distribution along the line of sight (Fig. 7, bottom middle plot), although formally the value of h_4 in this pixel falls into negative minimum.

At smaller inclinations ($i = 20^\circ - 40^\circ$), pixels with negative values of h_4 along the bar major axis are located approximately in the same area as for the face-on view (Fig 4, left column), especially considering that the negative minimum of h_4 for the face-on view is quite wide. This is clearly seen in the cuts along the major axis for different inclinations (Fig. 5, left column, solid lines). As mentioned above, the position of the formal negative minimum of h_4 moves outward. At the same time, at $i = 20^\circ$, in the region of the negative minimum of h_4 , there are still pixels with negative values of d_4 along the major axis, and there is a pronounced negative minimum of d_4 , although it does not coincide with the position of the h_4 minimum. At $i = 40^\circ$, pixels with negative values of d_4 disappear

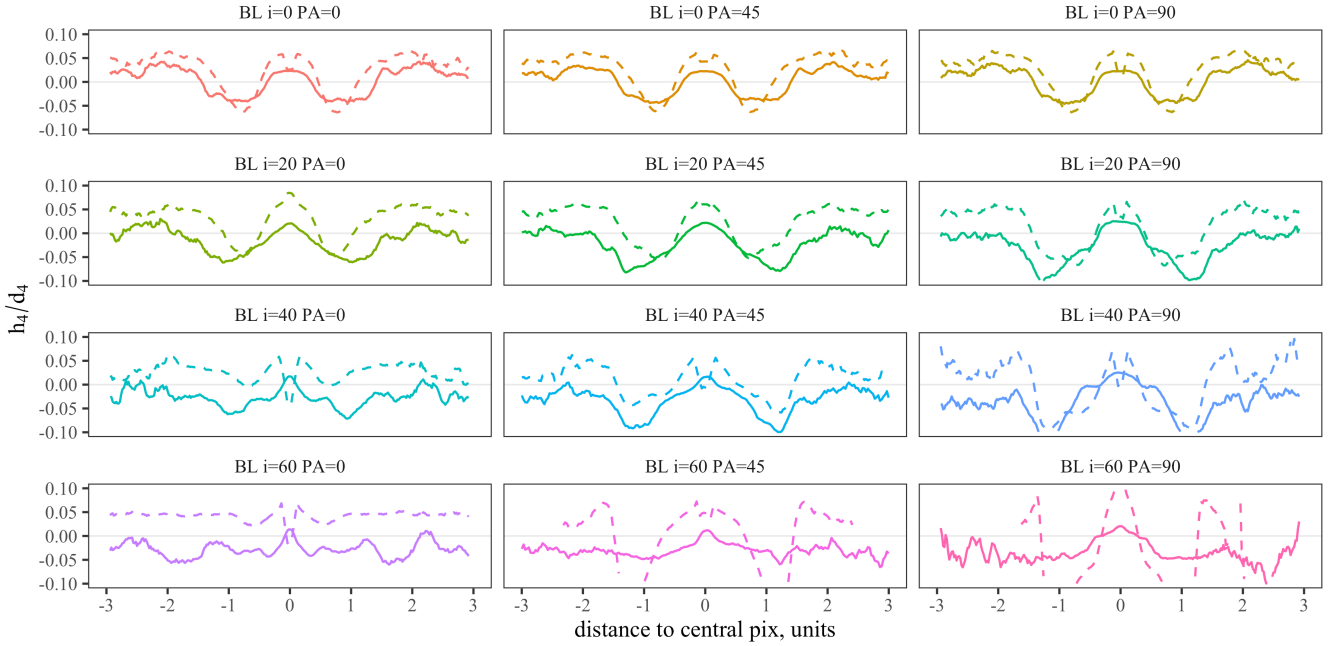


Figure 5. The h_4 (solid lines) and d_4 (dashed lines) profiles along the major axis for the BL model at different values of i and PA.

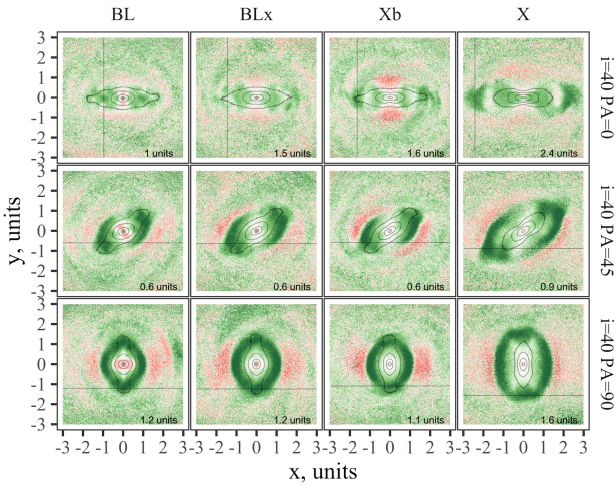


Figure 6. Differences between h_4 maps for all models (BL, BLx, Xb, X) at intermediate inclination $i = 40^\circ$ and varying position angles. The isophotes correspond to the intensity maps for a given position of the model relative to the observer. The vertical lines in the top row indicate the positions of h_4 minima along the major axis. The exact numbers at the bottom right corner of each panel show the distance from the centre of the model galaxy to the h_4 minima. The colors are the same as in Fig. 2.

completely, and the negative minimum of h_4 is strongly blurred in the B/PS bulge region. This means that for the low inclinations ($i < 40^\circ$) and PA = 0, negative values of h_4 along the major axis carry the information about the presence of a peanut despite the contamination of the LOSVD with the v_φ velocity component. However, this is no longer the case for larger inclinations of the galaxy even on the major axis of the bar.

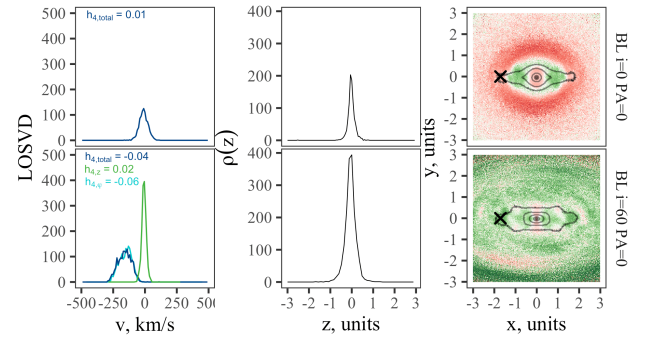


Figure 7. Left: LOSVDs for the pixel $(-1.7; 0)$ of the BL model at face-on position (top) and for the same model but inclined at $i = 60^\circ$ (bottom) with respect to the bar major axis. The total LOSVD (dark blue color) was additionally decomposed into vertical (v_z , green color) and azimuthal (v_φ , cyan) components. The selected pixel corresponds to the h_4 minima along the major axis for the BL model at $i = 60^\circ$. Centre: the vertical density distribution for both inclinations. Right: h_4 maps for $i = 0^\circ$ (top) and $i = 60^\circ$ (bottom). The isophotes (black lines) correspond to the intensity maps for a given inclination. The cross symbols show the position of selected pixels.

4.2 Contamination of LOSVD by radial velocity component

Our second example is the contamination of the LOSVD by the radial velocity components. For the BL model, we choose the pixel at the bar major axis at the distance of 1.57 units from the centre. Fig. 5 (upper right plot, solid line) and Fig. 9 (upper right plot, a cross in a red area) demonstrate a small positive value of h_4 in this pixel. The distribution function $f(v_z)$ in this pixel has a narrow peak around zero (Fig. 9, upper left plot) and corresponds to a narrow density distribution in the vertical direction (Fig. 9, upper middle

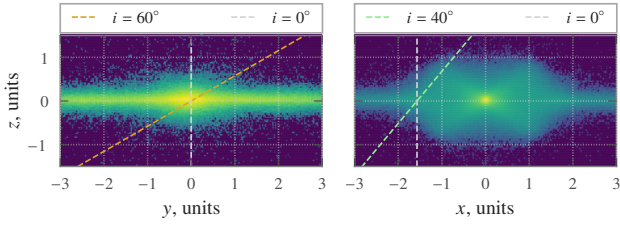


Figure 8. *Left:* a (yz) projection of the region selected by $|x + 1.7| < 0.02$ (i.e., a thin layer); LOS rays have angles $i = 0^\circ$ (light gray) and $i = 60^\circ$ (orange) and pass through the zero point of this view. *Right:* an (xz) projection of the layer $|y| < 0.02$; LOS rays have angles $i = 0^\circ$ (light gray) and $i = 40^\circ$ (light green) and pass through the point $(x, z) = (-1.57, 0)$.

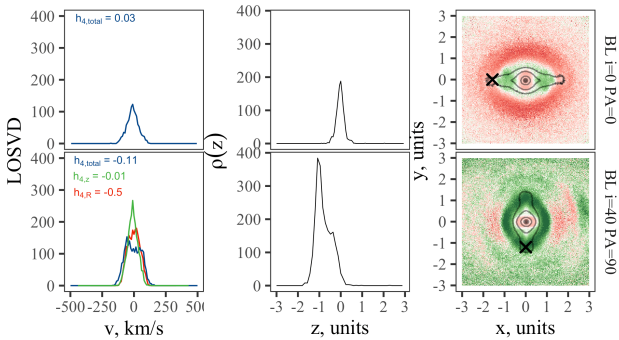


Figure 9. *Left:* LOSVDs for the pixel $(-1.2; 0)$ of the BL model at face-on position (top) and for the same model but inclined by $i = 40^\circ$ and rotated up to $PA = 90^\circ$ (bottom). The total LOSVD (dark blue color) was additionally decomposed into vertical (v_z , green color) and radial (v_R , red) components. The selected pixel corresponds to the h_4 minima along the major axis for the BL model at $i = 40^\circ$, $PA = 90^\circ$. *Centre:* the vertical density distribution for both cases. *Right:* h_4 maps for $i = 0^\circ$ (top) and $i = 40^\circ$, $PA = 90^\circ$ (bottom). The isophotes (black lines) correspond to the intensity maps for a given inclination. The cross symbols show the position of selected pixels.

plot) since the line of sight passes exclusively through the peripheral rather thin parts of the bar (Fig. 8, right plot, light grey line).

The inclination of the stellar disc around the minor axis of the bar by $i = 40^\circ$ shifts the positions along the major axis of the bar and reduces the distances due to projection effects. Thus, the selected pixel ends up at the distance of 1.2 units from the centre and falls into a deep negative minimum of h_4 (Fig. 5, right column, solid line, $i = 40^\circ$ and Fig. 9, bottom right plot, a cross in a dark green area). Now, two velocity components, v_R and v_z contribute to the LOSVD (Fig. 9, bottom left plot), and the features of the LOSVD are determined by the features of the radial velocity component distribution function $f(v_R)$. At the same time, the distribution function $f(v_z)$ remains narrow, although the line of sight in the upper half-plane of the B/PS bulge passes partially through its loose parts (Fig. 8, right plot, light green line). This is reflected in the skewed density distribution in the vertical direction (Fig. 9, bottom middle plot). Such a distribution has a negative value of the parameter d_4 (Fig. 5, right column, dashed line, $i = 40^\circ$). Additional particles from the loose region have almost no effect on $f(v_z)$, but they broaden the distribution $f(v_R)$ since particles located in a wide range of distances from the centre make an additional contribution to it.

At $i = 40^\circ$ and $PA = 90^\circ$, the B/PS bulge itself is located closer

to the centre from the negative minimum of h_4 along the major axis. In this region, there are many negative pixels of h_4 and d_4 for $i = 0^\circ$ which implies that the kinematic diagnostics of peanuts still works here, although the pixels themselves are not located at the very minimum of h_4 . Thus, at $PA = 90^\circ$ up to inclination $i = 40^\circ$, if we take a cut along the major axis of the bar we can assume that the negative minimum of h_4 points to the upper boundary of the B/PS bulge along the major axis (its tip).

For $i = 60^\circ$ and $PA = 90^\circ$, there is no formal negative minimum of h_4 along the major axis in the B/PS bulge region, and the cuts, as well as h_4 maps, are difficult to interpret.

5 ORBITAL GROUPS AND H_4

In this section, we discuss in detail the features of h_4 maps for all our models and contributions of various orbital components to the LOSVD (Section 2.2 contains information about the bar dissection into orbital groups). In Smirnov et al. (2021) and Tikhonenko et al. (2021), each of our models was disassembled into several orbital groups to analyse the face-on and edge-on morphology of an overall bar. We have excluded each orbital group in turn from the final model to determine how the h_4 maps change with the changes in the orbital groups that constitute the bar. These results should be interpreted with caution since such a simple removal of a particular orbital group does not eliminate the gravitational potential of these points in the rest of the model. This means that the influence of removed particles would be still imprinted in the kinematics of remaining particles and will show up in some way on the maps.⁷

For the face-on models, we analyse which orbital groups are responsible for peanut signatures on the h_4 maps. We now focus only on the BL and X models for a better example since the existence of the big bulges blurs the picture for the BLx and Xb models, albeit the reasons for the appearance of certain features on the h_4 maps are the same for all four models. The corresponding maps for the BLx and Xb models can be found in Appendix B.

5.1 Exclusion of orbital groups

Fig. 10 shows how the h_4 maps change when the orbits of each orbital group are excluded from the face-on snapshots for the BL and X models.

The BL model (upper row) consists of 55.49% particles of the disc, while around 45% belong to the bar component. The contributions of orbits supporting the bar are approximately equal between x1-like orbits (responsible for a narrow and elongated bar), boxy orbits (creating a face-on peanut), and bl₀ and bl_u orbits (main components of a barlens, Smirnov et al. 2021) — each group contributes about 10% of orbits (Table. 2). Although the bl₀ and bl_u orbits are the largest groups of orbits belonging to the bar and supporting the central barlens in the BL model, the exclusion of these types of orbits does not change the main features of the kinematic maps of h_4 . We only note changes on the minor axis, where the number of pixels with negative values decreased after the elimination of the bl₀ orbits. On the other side, when the x1 orbits are removed, almost all pixels with negative values of h_4 on the major axis disappear (upper row, the 2nd column of Fig. 10). Thus, the

⁷ As an example of such a pitfall, one may try to naively remove the thickest layers of the B/PS bulge only to find that face-on h_4 maps still look almost the same as they were for the original model.

characteristic minima of h_4 should be associated with the narrow and elongated bar and not with the barlens for the BL model. This result is consistent with the conclusions by [Tikhonenko et al. \(2021\)](#) obtained by analysing snapshots of various orbital subsystems, but here we use the kinematic analysis.

In its turn, the model with a pure face-on peanut bar (without a classical bulge and without a barlens, labelled X) mainly consists of disc (44.71%) and boxy orbits (45.19%). Accordingly, the elimination of boxy orbits for the X model removes almost all kinematic features in the centre of the model galaxy, along with four dark green rays with a small opening angle. All other groups of orbits in the bar are not represented in large numbers (only about 10% in total), and their exclusion has no effect on the h_4 maps.

For the BL model, a signal from pixels with negative values of d_4 is associated almost exclusively with x1 orbits. For the X model, on the contrary, a characteristic pattern in the area of the bar with negative values of the parameter d_4 is created by a subsystem assembled from boxy orbits. Thus, for models with different bar morphology, the features of the LOSVD expressed in term of h_4 parameter are formed by different orbits.

5.2 Exclusion of orbital groups from inclined models

In this section, we focus on a more detailed discussion of the formation of the ring of h_4 minima for barlens galaxies. As was discussed in previous sections, the ring of h_4 minima is not characteristic feature of galaxies with barlenses, and this ring is formed for all our models due to the contribution of azimuthal and radial velocity components to the LOSVD. In order to demonstrate that the pixels with negative values of h_4 on a face-on maps for inclined models have different nature, we now focus on the h_4 maps when the model has inclination $i = 40^\circ$ and the position angle $PA = 90^\circ$ (the most prominent ring). We will exclude the same orbital groups as in Section 5.1 from the model.

Fig. 11 (top row) shows the results for the BL model. The figure shows that exclusion of x1 orbits does not change the h_4 map⁸, although at $i = 0^\circ$ and $PA = 0^\circ$ the x1 orbits are responsible for the h_4 minima. The exclusion of the bl₀ orbits changes the map of h_4 , in contrast to the face-on case, producing some effect along the minor axis, but still not eliminating the ring.

The bottom row of the Fig. 11 shows the h_4 maps for the inclined X model. After eliminating the main orbital groups for the X model ('boxy' orbits), we also do not observe the elimination of the ring of h_4 minima⁹. Moreover, the exclusion of any type of orbits does not remove the ring.

Thus, we associate the ring of h_4 minima for $i > 20^\circ$ and $PA > 45^\circ$ not with the morphological features of the bar of one model or another, but with the contamination of the LOSVD by the velocity components v_φ or v_R . As was shown in Section 4, the main contribution to the LOSVD contamination for cuts along the major axis of the bar comes from the radial velocity component, if the galaxy is inclined around the minor axis of the bar. As to the minor axis, the appearance of the negative pixels comes from the azimuthal velocity component. Thus, we attribute the ring of h_4 minima for an inclined galaxy to a superposition of these two effects. For pixels in an intermediate position between the major and minor axes, the ring arises due to the contribution of all velocity

components to the LOSVD, but not due to the features of the vertical density distribution.

6 DISCUSSION

The kinematic maps presented in this work are well suited for interpreting IFU spectroscopy data. To date, one of the best spectral data on the kinematics of galaxies is the TIMER data. The galaxies of this sample (21 objects) have inclinations from $i = 20^\circ$ to $i = 60^\circ$ and a PA spread from 0° to 90° . Thus, to obtain an interpretation of these data, one needs a grid of N -body models at intermediate inclinations. However, [Debattista et al. \(2005\)](#) did not provide any maps with nonzero inclinations. They only briefly discussed the inclination effects for $i < 30^\circ$. [Bureau & Athanassoula \(2005\)](#) demonstrated the kinematic cuts, in particular, of the parameter h_4 (their Fig. 3), with different inclinations and PA (mainly $PA = 90^\circ$) but only for $i \geq 75^\circ$. [Iannuzzi & Athanassoula \(2015\)](#) also mainly discussed maps for models at high inclinations. Thus, our choice of inclinations ($0^\circ, 20^\circ, 40^\circ, 60^\circ$) and position angles ($0^\circ, 45^\circ, 90^\circ$) fill in the gap that exists in previous works. According to [Laurikainen & Salo \(2017\)](#), 11 from 17 clearly barred galaxies are also barlens galaxies in [Gadotti et al. \(2020\)](#) TIMER sample. One more galaxy (NGC 7755), which is not included in the sample by [Laurikainen & Salo \(2017\)](#), has clear photometric signs of a barlens on the S^4G image. To interpret such kinematic data, it is very important to have numerical models with a barlens. The models by [Debattista et al. \(2005\)](#) and [Bureau & Athanassoula \(2005\)](#) do not include a pure barlens. [Iannuzzi & Athanassoula \(2015\)](#) have barlens models (models GTR101 and GTR116), but there is no detailed map grid for such galaxies at intermediate inclinations. We provide these maps for our BL model with a barlens and demonstrate the kinematic features associated with this subsystem. Moreover, our wide grid of inclinations and position angles for all our models provide the possibilities to interpret not only MUSE data but also apply it for future spectroscopic surveys.

We have models that are close to the models analysed by [Debattista et al. \(2005\)](#), and using their example we can confirm the absence of a relationship between the extent of the B/PS bulge and the size of the area where the double negative minima of h_4 are localised. Our model X resembles the R1 and R4 models by [Debattista et al. \(2005\)](#) in the Toomre parameter Q and the initial thickness, although [Debattista et al. \(2005\)](#) considered models with rigid halos. The Xb model is analogous to the model B3 ($M_b/M_d = 0.2$, [Debattista et al. 2005](#)). As a result, the h_4 maps for the models X, Xb are similar to the maps of the parameter s_4 of [Debattista et al. \(2005\)](#) for their models R1, R4 and B3. The X model has the extended B/PS bulge, and the negative minima of h_4 are located close to the center and do not coincide with the thickest parts of the B/PS bulge, as it is seen on the side-on snapshots (Fig. 1). To some extent, this also applies to the Xb model. As was noted in the Section 3, the negative values of the h_4 parameter are also partially localised in the bar itself away the minima on the major axis along four rays and outline the dimensions of the B/PS bulge. The models by [Debattista et al. \(2005\)](#), similar to the X and Xb models, exhibit the same behavior (e.g., the rightmost panel of their Fig. 13). This means that although the B/PS bulge is usually associated with the thickest parts of the bar, the parameter h_4 does not always delineate the boundaries of these thickest areas if we take cuts along the major axis. In Section 6.1 we will discuss in more details the relationship between the bar thickness, vertical density distribution, and kinematic signatures of a peanut.

⁸ The same area as for $i = 0^\circ$ and $PA = 0^\circ$ case in Section 5.1.

⁹ Although we note that there are practically no particles in this region.

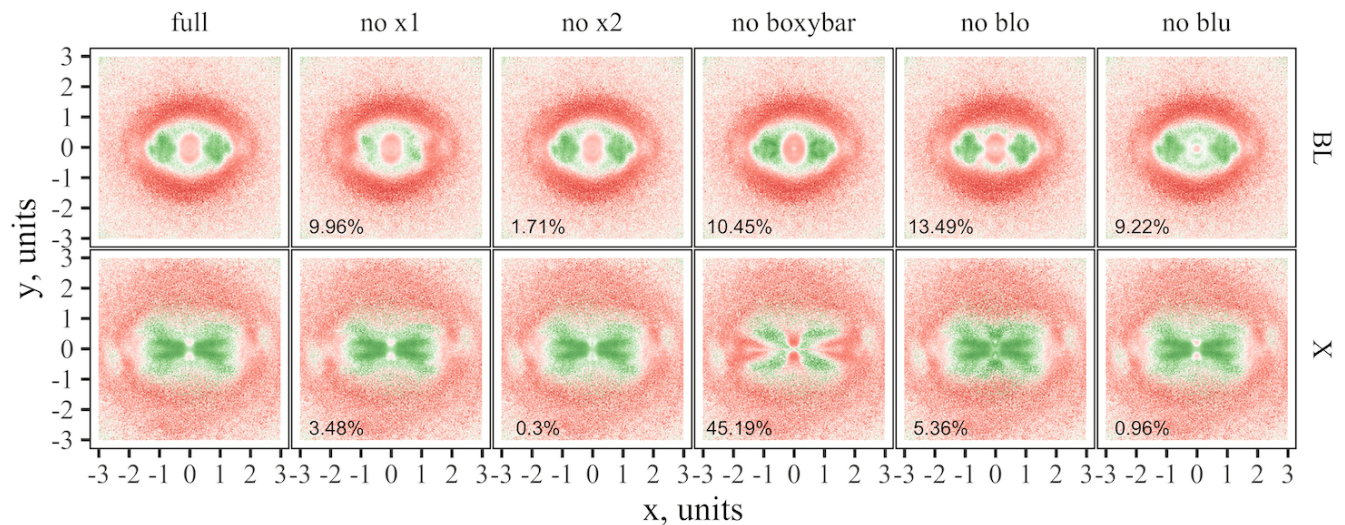


Figure 10. The maps of h_4 for the BL (top row) and X (bottom row) models at face-on position with orbital groups excluded in turn. The numbers in the bottom left corner of each plot correspond to the relative contribution of the currently excluded orbital group (indicated in the title of each plot) to the total number of particles (see Table 2 for details). The colors are the same as in the Fig. 2.

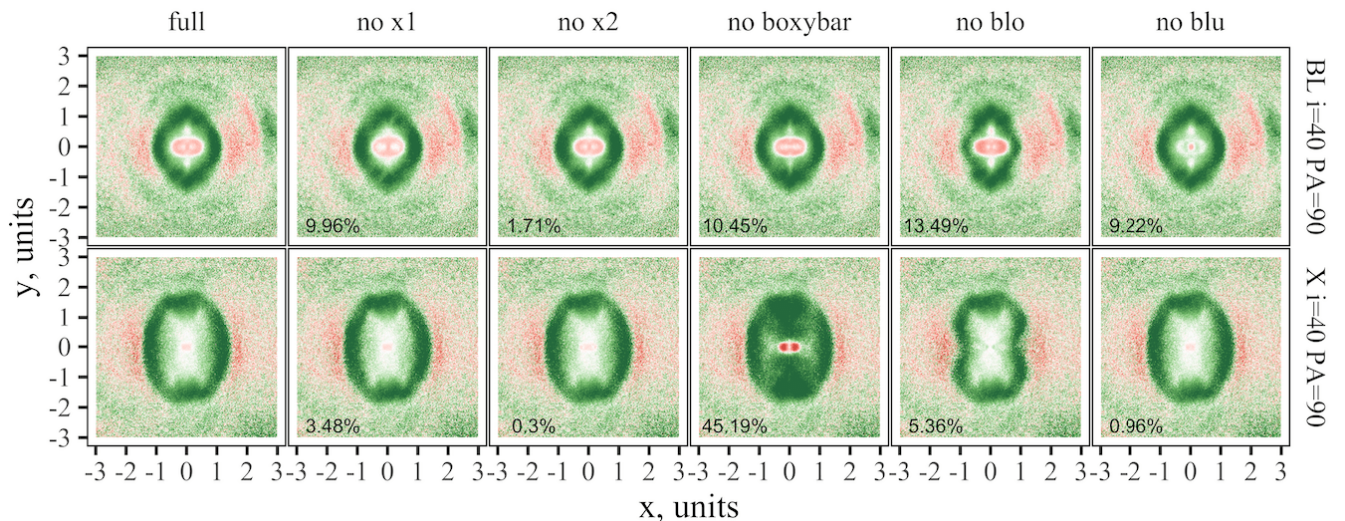


Figure 11. The same maps of h_4 for the BL (top row) and X (bottom row) models as in Fig. 10 but for $i = 40^\circ$ and $PA = 90^\circ$. Starting from the second column, a particular orbital group is excluded in each panel. The colors are the same as in Fig. 2.

One more feature on the h_4 maps, which is typical for all our models is the ring of negative values of h_4 when $PA > 45^\circ$. Signatures of a ring from negative values of h_4 can be noticed in figure 29 by Iannuzzi & Athanassoula (2015) (the case $PA = 90^\circ$, $i = 60^\circ$, models GTR101 and GTR116, which apparently have barlenses). This is the main plot which is used to interpret the TIMER data. As the appearance of a ring on the h_4 maps for our models is solely the effect of the galaxy inclination and a special value of the position angle of the bar major axis, in Section 6.2 we discuss the pitfalls regarding the interpretation of available observational kinematic maps. We also warn of difficulties regarding the interpretation of available observational kinematic maps.

6.1 How kinematics captures the density distribution

In Section 3.1, we have shown that for the models with B/PS bulges but with different bar morphology in a face-on view, the characteristic vertical density distribution of B/PS bulges (the values of d_4) is followed by the broadness of LOSVD (h_4 parameter). This result is in agreement with Debattista et al. (2005). Moreover, we have shown that negative values of h_4 follow only flat-topped distribution, but not the thickest parts (Fig. 2). For a more detailed analysis, we now discuss the behaviour of h_4 and d_4 values in the thickest areas of the bar (top 10% of the pixels sorted by $\text{med } |z|$). Fig. 12 shows that the thickest part of the galaxy is not characterised by a flat-topped density distribution and, respectively, by negative values of h_4 . Also, Fig. 12 demonstrates that in the thickest regions of the bar, the most

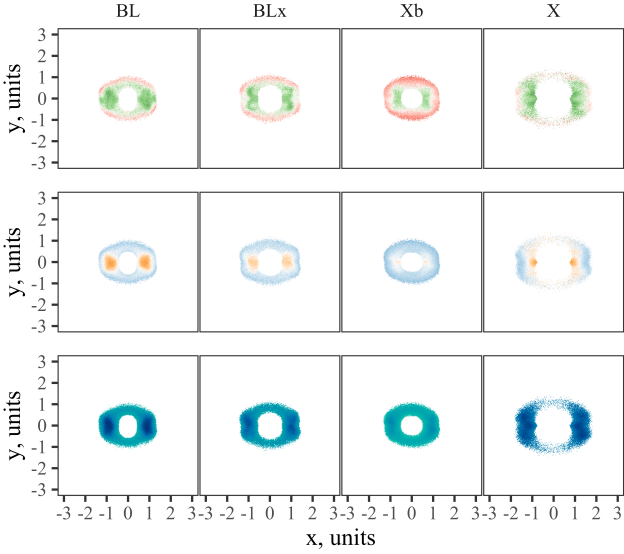


Figure 12. The maps of h_4 (top row), d_4 (middle row) and $\text{med } |z|$ (bottom row) for the BL, BLx, Xb, and X models (from the left to the right) in the thickest area of the bar (top 10% of the pixels sorted by $\text{med } |z|$). The colors are the same as in Fig. 2.

negative values of h_4 and d_4 are localised in the same places for all models. At least, this is true for pixels lying in a strip along the major axis of the bar. At the same time, there is no connection between the kinematics (h_4 , the top row of Fig. 12) and the thickness of the models (bottom row of Fig. 12). All considered models show both positive and negative h_4 values in these selected pixels. The h_4 minima do not fall into the regions of the largest thickness for the BLx and Xb models, especially for the X model, although for the BL model, the h_4 minima are located in the pixels that characterise the largest thickness. Fig. 13 shows the relationships between three parameters, h_4 , d_4 and $\text{med } |z|$, for the pixels in the thickest areas of the bar (10% of the pixels with the largest thickness values). In the thickest zones, a clear anticorrelation between h_4 and $\text{med } |z|$ exists only for the BL model.

For the thickest parts of the bar in models without a barlens, the minima of h_4 and d_4 shift from the centre to the periphery (compare Fig. 2 and Fig. 12). In the X model, the prevailing orbits in the bar are boxy orbits, which, unlike x1 orbits, have many self-intersections near the centre. They give deep two-sided minima of h_4 near the centre on the maps in Fig. 2, although these areas are not thickest. For the thickest areas of the bar, the positions of the double minima of h_4 and d_4 are very similar for all models. We refer it to the fact that the minima for our X model are very wide and the negative values of h_4 are still present within boundary of the most vertically extended B/PS bulge part (see Fig. 1).

Thus, although the flat-topped shape of the LOSVD (negative values of h_4) in the face-on case for models with different types of B/PS bulges does not unambiguously track the thickest areas of the B/PS bulges, in the thickest regions, the h_4 parameter certainly is an indicator of the features of the vertical density distribution (d_4). It follows that interpretation of the real data has to be done carefully since the minima of h_4 do not track the position of the thickest zones and, accordingly, do not track the size of the B/PS bulge.

The h_4 parameter reliably tracks the vertical density distribution only in the face-on case. As the inclination increases, other

velocity components (v_φ and v_R) contaminate the LOSVD, and h_4 no longer follows d_4 . Thus, for inclined galaxies, the analysis of the shape of the LOSVD as an indicator of a peanut should be carried out with caution because at $i \geq 40^\circ$ the connection between h_4 and d_4 is broken (Fig. 5). There is another effect associated with the broadness of LOSVD. Differently rotating components (for example, disc and bar) also lead to a negative value of the parameter h_4 , but this has nothing to do with the features of the vertical density distribution. Such effects also may contaminate the h_4 maps of inclined galaxies. We have shown that for all our models with B/PS bulges, the effects of inclination and rotation of the bar major axis affect the h_4 maps similarly. Accordingly, we conclude that there are no significant differences in kinematics between different types of B/PS bulges in our models.

6.2 Possible pitfalls in interpreting observational data

The h_4 parameter reliably tracks the vertical density distribution only in the face-on case. However, even for galaxies with low inclinations and low PA (as in the two upper plots on the left of Fig. 4 and Fig. 5), interpreting the two-sided minima of h_4 along the major axis of a bar is sophisticated. The reasonable question is, which component of the bar these minima can be attributed to as the signatures of a B/PS bulge, i. e. to the bar itself or to the barlens if each of them is present, as in galaxy NGC 98 (Méndez-Abreu et al. 2008, 2014). The analysis of the orbital composition of the bar carried out in Section 5.1 showed that for the BL model, only the component assembled from the x1 orbits shows the peanut signatures. Inclusion in or exclusion from the model of orbits assembled into a barlens (bl_o and bl_i) has no effect on the h_4 maps (Fig. 10). Signatures of a peanut, as a two-sided minima of h_4 on the major axis of the bar, are always present, but they are not related to the barlens.

The most demanded in kinematic applications may be our BL model, although all our models show similar behaviour when the galaxy is inclined and rotated. We refer to the fact that all our models are galaxies with B/PS bulges. The question arises whether, it is possible to say that the edge-on B/PS bulge in the BL model is identical to the face-on barlens based on the kinematics. For galaxies with $i > 20^\circ$ and $\text{PA} > 45^\circ$, our models predict a ‘ring’ of negative values of h_4 . The appearance of the ring in h_4 maps is consistent with the h_4 maps of the inclined galaxies NGC 4984 and NGC 7755 ($\text{PA} \approx 90^\circ$) from Gadotti et al. (2020). As an illustration, we show the h_4 maps from Gadotti et al. (2020) and model maps created from the BL model in Fig. 14. The model was positioned in the same way relative to an observer as the galaxies in question.

However, the presence of the ring of negative values of the parameter h_4 is not an exclusive feature of the BL model. With this position of the bar, the ring appears for all our models. The existence of such a ring is not a signature of a peanut. It is associated with the complicated contribution of other velocity components, v_R and v_φ , to the LOSVD, in addition to v_z . As we have shown above, a signature of the B/PS bulge through the h_4 parameter appears only along the major axis for low inclinations of the galaxy.

We stress that this work is primarily dedicated to the detection of the vertical density distribution features from the stellar kinematics. To make our point clear, we focus on the values of the h_4 parameter alone for now. However, the LOSVDs of the models contain a lot of information, for example, we do not use the ‘skewness’ of the LOSVD (the h_3 parameter). In Sec. 3.1 and 3.3, we do find a minor difference in the h_4 maps depending on the model, but eventually conclude that these differences are insufficient to clearly distinguish them. This situation changes when one starts consid-

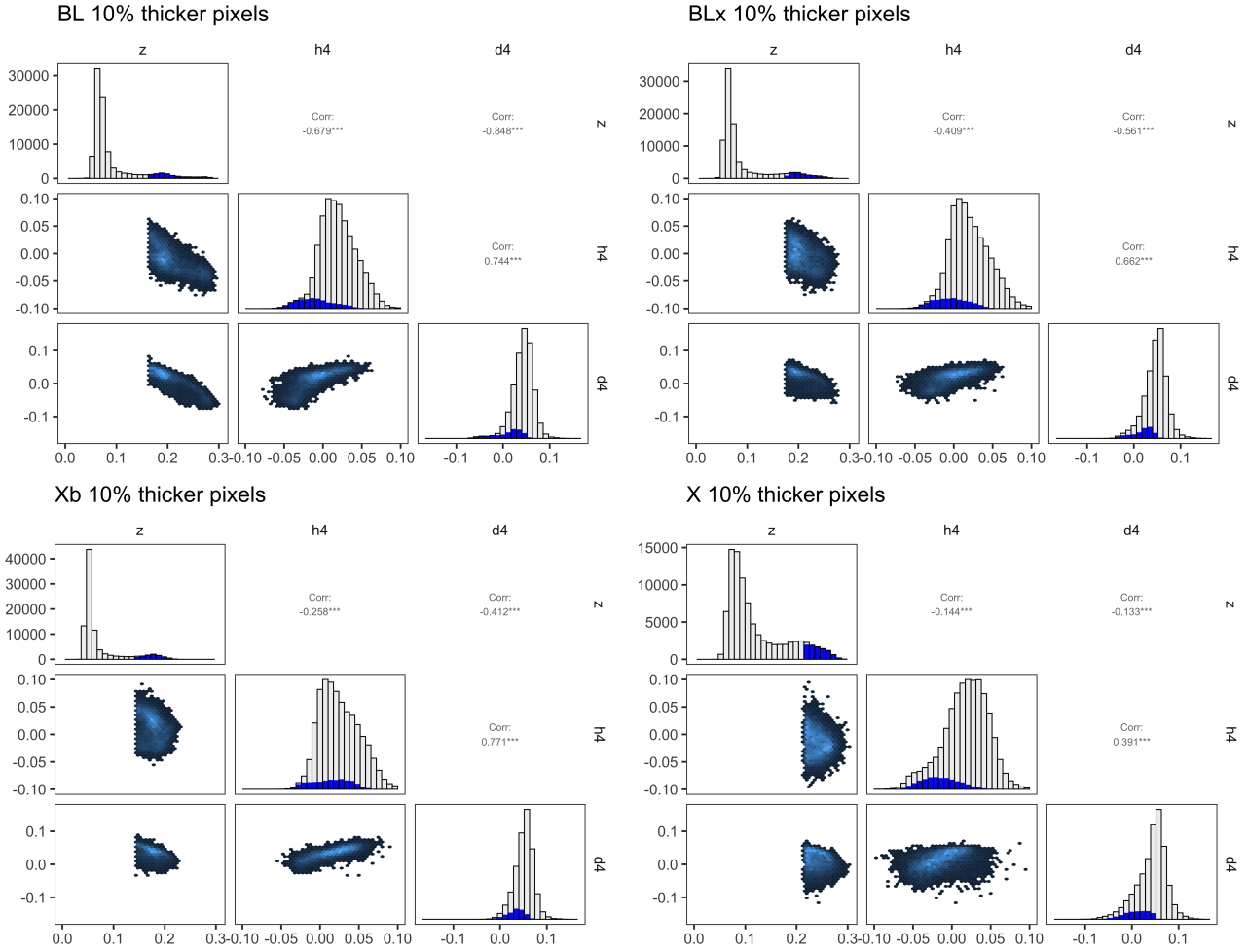


Figure 13. The correlation matrix between h_4 , d_4 , and $\text{med } |z|$ for the thickest areas of the bar (top 10% of the pixels sorted by $\text{med } |z|$), according to Fig. 12

ering the h_3 parameter too. In Fig. 15, we provide preliminary h_3 maps for all our models, where one can see that the BL model has a distinctive feature in its central part (inside 0.5 units radius). This feature is associated with the rotation of the inner parts of the barlens but does not characterize its vertical structure. We tentatively connect this feature with bl_in component, which is also responsible for the slightly elevated h_4 values in the same area (cf. the rightmost and the leftmost panels of the Fig. 10), ultimately leaving the problem of the detection of kinematic characteristics of barlens galaxies using both h_3 and h_4 parameters to a future paper focused on a more detailed comparison of BL model kinematics with available observational data.

7 CONCLUSIONS

We have explored four N -body models that have a gradual progression in a face-on bar morphology and imitate real galaxies from galaxies with a barlens to featureless barred galaxies. Like our predecessors (Debattista et al. 2005; Iannuzzi & Athanassoula 2015), we focused on the analysis of 2D maps of the h_4 parameter to probe the presence of a “peanut” in cases where this morphological feature is not visually evident. These maps, produced on the basis of model data cubes with a spectral resolution close to that available, for example, for the data from the TIMER project (Gadotti et al. 2019),

can be compared with real observational data. We have studied in detail the 2D kinematic maps for various orientations of the bar to the line of sight ($i = 0^\circ - 60^\circ$, $\text{PA} = 0^\circ - 90^\circ$). Our uniform grid of disc inclinations and position angles of the bar major axis covers almost all possible variations in the position of the galaxy, except for the edge-on view.

Based on the spectral analysis of the main frequencies of the orbits in the bar, we have previously identified separate subsystems, or orbital groups, assembled into a bar (Smirnov et al. 2021). The groups differ in structure, primarily vertical, which means that they can also differ kinematically. We have analysed the contributions of the LOSVDs of individual orbital components to the cumulative LOSVD in order to correctly interpret the LOSVD moment maps and judge which orbital groups make the main contribution to the negative values of the parameter h_4 .

The main conclusions of the work are as follows.

1. The characteristic vertical density distribution attributed to the B/PS bulges subsists in models with and without barlens and can be detected using the parameter h_4 .
2. The data analysed to reproduce the well-established face-on kinematic signatures of the presence of a “peanut” (B/PS bulge): at low inclinations ($i < 20^\circ$) along the major axis of the bar, two symmetrical negative minima of the h_4 parameter are observed. Unlike other negative pixels on the 2D maps of the h_4 parameter,

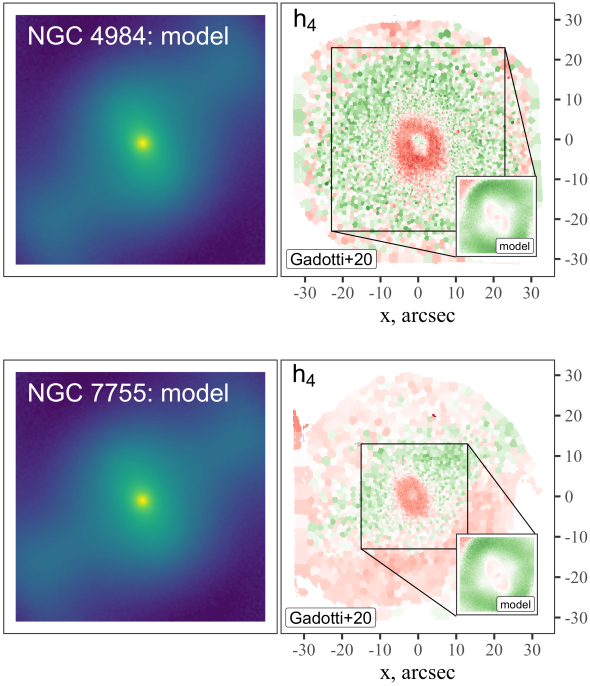


Figure 14. The BL model rotated to mimic two galaxies from the TIMER sample: NGC 4984 (*top plot*, $i = 54^\circ$, $PA = -103^\circ$) and NGC 7755 (*bottom plot*, $i = 53^\circ$, $PA = 94^\circ$). For each plot, the *left panel* shows the intensity map of the model. On *right panels* we reproduce the maps of h_4 parameter from Gadotti et al. (2020) with synthetic h_4 maps of our BL model shown on the inset plots. The h_4 colourbar is the same as in Fig. 2.

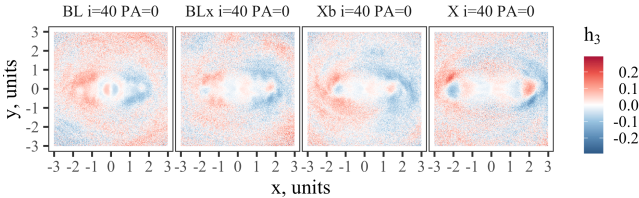


Figure 15. The preliminary maps of h_3 parameter for all considered models at $PA = 0^\circ$, $i = 40^\circ$

the negative pixels of this parameter along the major axis of the bar really delineate the boundaries of the B/PS bulge.

3. There are no significant morphological differences in the maps of the h_4 parameter for the model with a barlens (BL model) and without it (X model) at all inclinations and $PA > 45^\circ$, when a ring of negative h_4 values begins to form. An interpretation of observational data at this viewing position of the galaxy only on the basis of these maps does not allow one to probe the vertical structure of a barlens if it is present and co-exists with a B/PS bulge within the same galaxy.

4. With an increased inclination, the diagnostics based on the h_4 parameter is ruined due to a break in the connection of the h_4 parameter with the features of the vertical density distribution.

5. We clearly distinguish between the influence of two factors on the morphology of the LOSVD moment maps. The first is the effect of the inclination (contamination of the LOSVD with velocity projections other than v_z). The second is the contamination of the

cumulative LOSVD by the LOSVDs of different orbital subsystems or with different kinematics (fast and slow rotating components).

6. The wide ring of negative values of h_4 is observed on 2D model maps at intermediate inclinations ($i = 20^\circ - 60^\circ$) and $PA > 45^\circ$. Such rings can be noticed on the h_4 maps for the barlens galaxies (e.g., NGC 3351, NGC 4984, NGC 7755, Gadotti et al. 2020). However, rings are present in all our models, and their appearance can not be a distinguishing feature of the barlens model.

7. We analysed the impact of different orbital groups in the bar on the kinematic signatures of a peanut for all our models. For our models, different orbital groups make different contributions to the minima of h_4 on both sides along the major axis of the bar. For the barlens model, the minima of h_4 are associated with the x1 family of orbits, the main building material of a long narrow bar. If this orbital family is well represented in the bar, then it is this family that will give two-sided negative minima of h_4 along the major axis of the bar and signals about the features of the vertical density distribution (B/PS bulge). Thus, the orbits supporting the barlens are not responsible for the kinematic signatures of the peanut.

ACKNOWLEDGEMENTS

The authors express gratitude for the financial support from the Russian Science Foundation (grant no. 22-22-00376). We are grateful to the anonymous reviewer for a careful and thorough reading of the manuscript. We are also grateful to the TIMER team (Gadotti et al. 2019) for making their data publicly available. This work made use of Astropy¹⁰ a community-developed core Python package and an ecosystem of tools and resources for astronomy (Astropy Collaboration et al. 2013, 2018, 2022), as well as NEMO stellar dynamics toolbox (Teuben 1995). The authors also thank Roberto Saglia for reading a preliminary version of this manuscript and a fruitful discussion regarding the optimal way to present the results of this work.

8 DATA AVAILABILITY

The data underlying this article be shared on reasonable request to the corresponding author.

REFERENCES

- Astropy Collaboration et al., 2013, *A&A*, **558**, A33
 Astropy Collaboration et al., 2018, *AJ*, **156**, 123
 Astropy Collaboration et al., 2022, *apj*, **935**, 167
 Athanassoula E., 2016, in Laurikainen E., Peletier R., Gadotti D., eds, *Astrophysics and Space Science Library Vol. 418, Galactic Bulges*. p. 391 ([arXiv:1503.04804](https://arxiv.org/abs/1503.04804)), doi:10.1007/978-3-319-19378-6_14
 Athanassoula E., Laurikainen E., Salo H., Bosma A., 2015, *MNRAS*, **454**, 3843
 Binney J., Spergel D., 1982, *ApJ*, **252**, 308
 Bittner A., et al., 2019, *A&A*, **628**, A117
 Brown J. S., Valluri M., Shen J., Debattista V. P., 2013, *ApJ*, **778**, 151
 Bureau M., Athanassoula E., 2005, *ApJ*, **626**, 159
 Cappellari M., Emsellem E., 2004, *PASP*, **116**, 138
 Combes F., Sanders R. H., 1981, *A&A*, **96**, 164
 Debattista V. P., Carollo C. M., Mayer L., Moore B., 2005, *ApJ*, **628**, 678
 Dehnen W., 2002, *Journal of Computational Physics*, **179**, 27

¹⁰ <http://www.astropy.org>

- Erwin P., Debattista V. P., 2013, *MNRAS*, 431, 3060
 Erwin P., Debattista V. P., 2017, *MNRAS*, 468, 2058
 Gadotti D. A., et al., 2019, *MNRAS*, 482, 506
 Gadotti D. A., et al., 2020, *A&A*, 643, A14
 Gerhard O. E., 1993, *MNRAS*, 265, 213
 Hernquist L., 1990, *ApJ*, 356, 359
 Iannuzzi F., Athanassoula E., 2015, *MNRAS*, 450, 2514
 Kormendy J., 1979, *ApJ*, 227, 714
 Laurikainen E., Salo H., 2016, in Laurikainen E., Peletier R., Gadotti D., eds, *Astrophysics and Space Science Library* Vol. 418, Galactic Bulges. p. 77 ([arXiv:1505.00590](https://arxiv.org/abs/1505.00590)), doi:10.1007/978-3-319-19378-6_4
 Laurikainen E., Salo H., 2017, *A&A*, 598, A10
 Laurikainen E., Salo H., Buta R., Knapen J. H., 2011, *MNRAS*, 418, 1452
 Laurikainen E., Salo H., Athanassoula E., Bosma A., Herrera-Endoqui M., 2014, *MNRAS*, 444, L80
 Laurikainen E., Salo H., Laine J., Janz J., 2018, *A&A*, 618, A34
 Li Z.-Y., Ho L. C., Barth A. J., 2017, *ApJ*, 845, 87
 Lütticke R., Dettmar R.-J., Pohlen M., 2000a, *A&AS*, 145, 405
 Lütticke R., Dettmar R. J., Pohlen M., 2000b, *A&A*, 362, 435
 Marinova I., Jogee S., 2007, *ApJ*, 659, 1176
 McMillan P. J., Dehnen W., 2007, *MNRAS*, 378, 541
 Méndez-Abreu J., Corsini E. M., Debattista V. P., De Rijcke S., Aguerri J. A. L., Pizzella A., 2008, *ApJ*, 679, L73
 Méndez-Abreu J., Debattista V. P., Corsini E. M., Aguerri J. A. L., 2014, *A&A*, 572, A25
 Navarro J. F., Frenk C. S., White S. D. M., 1996, *ApJ*, 462, 563
 Parul H. D., Smirnov A. A., Sotnikova N. Y., 2020, arXiv e-prints, p. arXiv:2002.06627
 Salo H., Laurikainen E., 2017, *ApJ*, 835, 252
 Smirnov A. A., Tikhonenko I. S., Sotnikova N. Y., 2021, *MNRAS*, 502, 4689
 Teuben P., 1995, in Shaw R. A., Payne H. E., Hayes J. J. E., eds, *Astronomical Society of the Pacific Conference Series* Vol. 77, *Astronomical Data Analysis Software and Systems IV*. p. 398
 Tikhonenko I. S., Smirnov A. A., Sotnikova N. Y., 2021, *A&A*, 648, L4
 Valluri M., Shen J., Abbott C., Debattista V. P., 2016, *ApJ*, 818, 141
 van der Marel R. P., Franx M., 1993, *ApJ*, 407, 525

APPENDIX A: EFFECTS OF INCLINATION: h_4 MAPS

In Section 3.2, we provide the h_4 maps for different inclinations and position angles for the BL model. Figs. A1, A2, A3 show the maps similar to those presented in Fig. 4, for the BLx, Xb, and X models. Despite the differences between h_4 maps for a face-on view, which depend on the exact bar morphology, the inclination effects are similar and lead to the same kinematic features for all presented B/PS bulges. As was shown in the Sections 3.2, 3.3, 5, 5.2 all B/PS bulges form the rings of h_4 minima for $i > 20^\circ$ and $PA > 45^\circ$. We also note that the size of the ring depends on the exact size of the B/PS bulge.

APPENDIX B: DISSECTION OF THE BAR INTO ORBITAL GROUPS FOR BLX AND XB MODEL

Section 5 contains the h_4 maps for the BL and X models. Here we provide the same maps for the BLx and Xb models. Both of them mainly consist of a quarter of boxy orbits, which contribute to the h_4 maps in the face-on case (Fig. B1). However this contribution is hardly to notice. We refer it to the smearing of the peanut signatures by the classical bulge in the centre (for the BL model the classical bulge is compact, the X model has no a classical bulge). Fig. B2 shows that the exclusion of any of orbital group of the bar does not change the h_4 maps for the inclined galaxies.

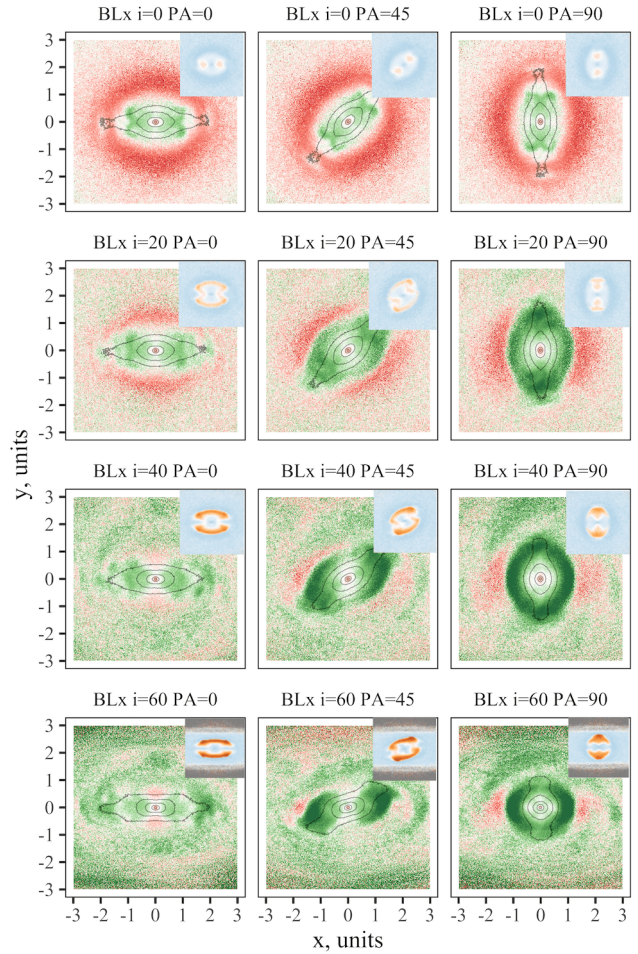


Figure A1. Effects of the disc inclination (i) and PA in the h_4 maps for the BLx model. See Fig. 4 for all details.

This paper has been typeset from a $\text{\TeX}/\text{\LaTeX}$ file prepared by the author.

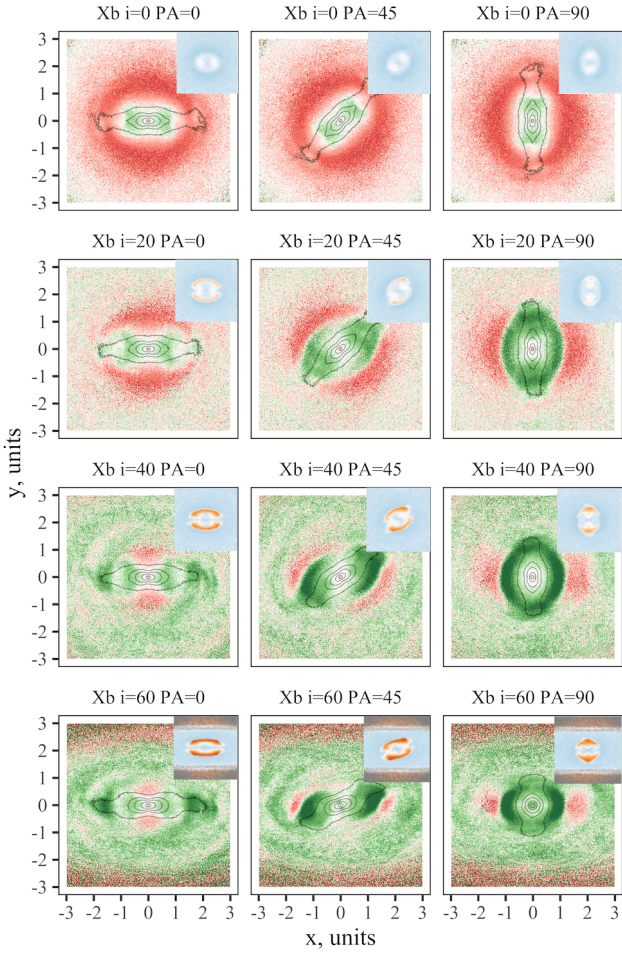


Figure A2. Effects of the disc inclination (i) and PA in the h_4 maps for the Xb model. See Fig. 4 for all details.

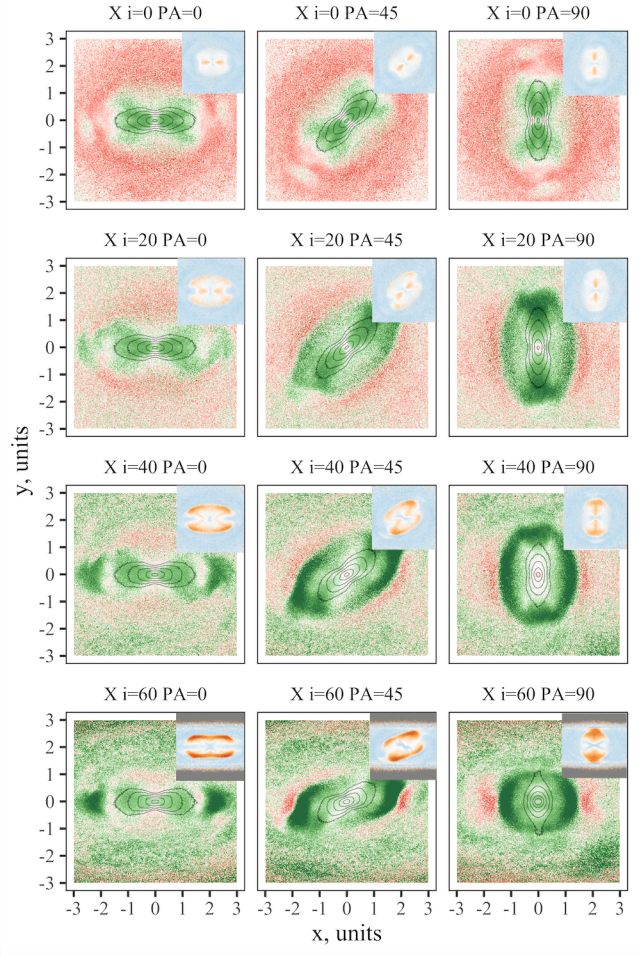


Figure A3. Effects of the disc inclination (i) and PA in the h_4 maps for the X model. See Fig. 4 for all details.

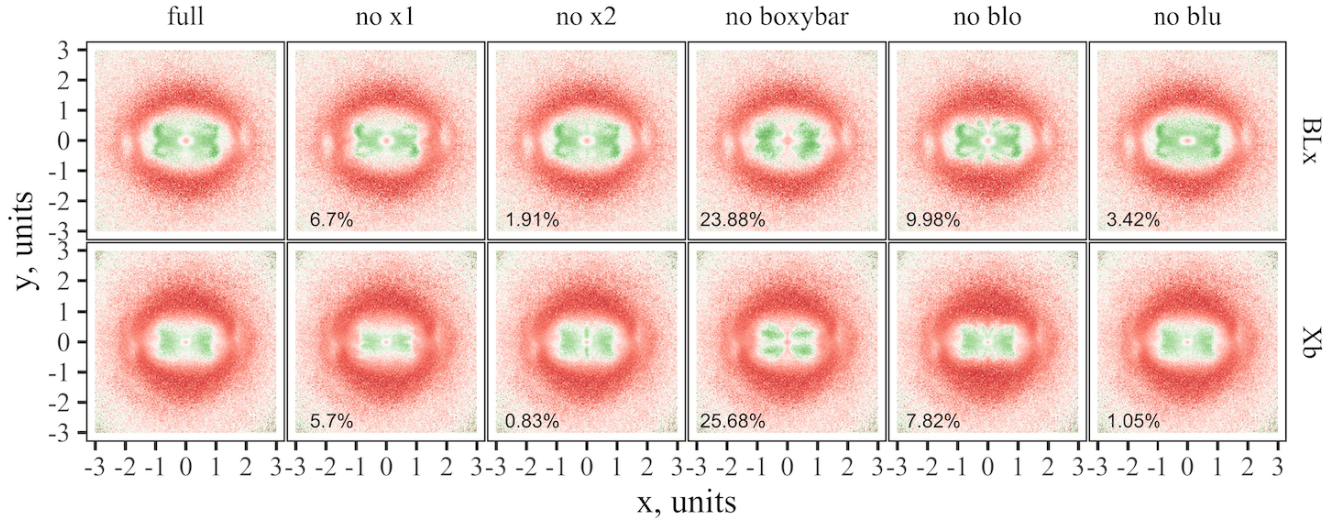


Figure B1. The maps of h_4 for the BLx (top row) and Xb (bottom row) models at face-on position with orbital groups excluded in turn. See Fig. 10 for all details.

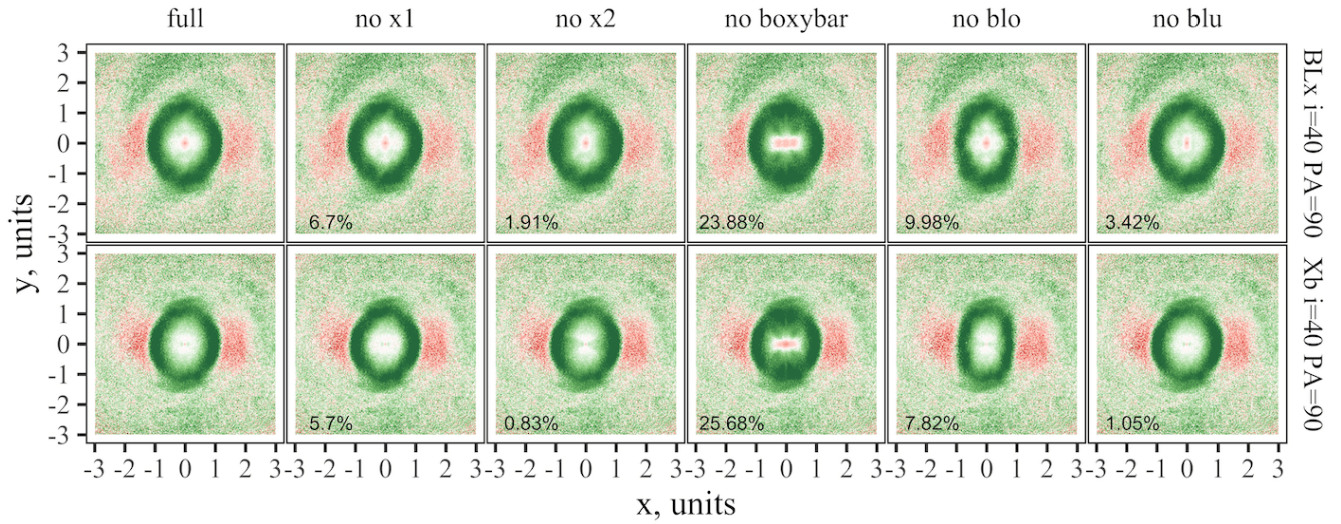


Figure B2. The maps of h_4 for the BLx (top row) and Xb (bottom row) models at $i = 40^\circ$, PA = 90° with orbital groups excluded in turn. See Fig. 11 for all details.